Acta Materialia 194 (2020) 118–133

Contents lists available at ScienceDirect

Acta Materialia

journal homepage: www.elsevier.com/locate/actamat

Full length article

Quantification of hydrogen trapping in multiphase steels: Part I – Point traps in martensite

Andrej Turk[a,d], Gaurav R. Joshi[c], Marius Gintalas[e], Mauro Callisti[a], Pedro E.J. Rivera-Díaz-del-Castillo[b], Enrique I. Galindo-Nava[*,a]

[a] Department of Materials Science and Metallurgy, University of Cambridge, 27 Charles Babbage Road, Cambridge CB3 0FS, United Kingdom
[b] Department of Engineering, Lancaster University, Gillow Ave, Bailrigg, Lancaster LA1 4YW, United Kingdom
[c] School of Materials, University of Manchester, Sackville Street Building, Manchester M1 3WE, United Kingdom
[d] OxMet Technologies Ltd, Unit 15, Oxford Business Park, Yarnton, Kidlington OX5 1QU, United Kingdom
[e] Department of Mechanical and Aerospace Engineering, NSIRC, Brunel University London, Cambridge CB21 6AL, United Kingdom

ARTICLE INFO

Article History:
Received 8 October 2019
Revised 24 April 2020
Accepted 4 May 2020
Available online 16 May 2020

Keywords:
Hydrogen diffusion
Austenite
Dislocation density
Grain boundaries
Thermal desorption analysis (TDA)

ABSTRACT

We quantified systematically the H trap density in martensite resulting from the presence of dislocations, grain boundaries and retained austenite through a combination of detailed microstructural characterisation, H permeation, thermal desorption and diffusion modelling. This thorough analysis allowed for the first time to deconvolve key microstructural constituents affecting H diffusion in multi-trap martensite. Three microstructures were investigated – as-quenched, tempered at 300 °C and tempered at 450 °C. The first two microstructures had identical dislocation densities and grain size, while the as-quenched one also contained 3.5 vol.% of retained austenite. The two tempered microstructures showed a large difference in dislocation density with few other microstructural differences. The as-quenched microstructure exhibited over an order of magnitude lower H diffusivity and increased H trapping due to retained austenite, while the tempered samples exhibited very similar diffusivities, indicating that dislocations have a limited effect on H trapping. Trap density scaling laws were successfully identified and validated through diffusion simulations and experiments. It was also shown that in martensite and heavily deformed ferrite, where the average grain size is small, grain boundaries are more effective trapping sites than dislocations. Our results also show that retained austenite cannot be effectively modelled as a point trap under the local equilibrium assumption, which is frequently used to model its effect on H diffusion, and that bulk trapping must be considered at least in two dimensions, which is addressed in part II of this series.

1. Introduction

H diffusion in steels is known to be very sensitive to microstructure [1,2], but while numerous experimental studies of H diffusivity and absorption properties of a variety of different microstructures have been performed to date (*e.g.* [3–6]), there have been few rigorous attempts at correlating the size and/or density of defects/constituent phases to the density of H trapping sites N_t and their average binding energy ΔE_t. This knowledge is key in designing alloys resistant to hydrogen embrittlement (HE). Current research shows that HE susceptibility is correlated to the concentration of freely diffusing H, or lattice hydrogen c_l, and its effective diffusivity in the material D_{eff} [7], both of which are functions of microstructure. HE is of particular concern in high-strength steels, which possess complex multi-phase microstructures generally based on mixtures of martensite and austenite. The large solubility and low diffusivity of H in the latter relative to martensite and ferrite means that the presence of even small amounts of austenite in a given steel may have a significant impact on the H diffusion rate. The effect is poorly understood, particularly from a modelling point of view, and only a handful of modelling studies on this topic exist, none of which have been tested against experimental data. One of the two main aims of this series of papers is to investigate the effect of austenite, its volume fraction and morphology on diffusion by a combination of experiments and simulations, partly discussed here but elaborated on in part II. The second main aim is to quantify the relationship between the most prominent defects in martensite, grain boundaries and dislocations, and their effect on H diffusion. The quantification of nano-scale precipitates has been examined in a previous work [8].

The ubiquity of martensite and its generally high susceptibility to HE has resulted in a vast body of literature on H diffusion and

* Corresponding author.
E-mail addresses: at712@cam.ac.uk (A. Turk), gauroba@gmail.com (G.R. Joshi), marius.gintalas@brunel.ac.uk (M. Gintalas), mc2057@cam.ac.uk (M. Callisti), p.rivera1@lancaster.ac.uk (P.E.J. Rivera-Díaz-del-Castillo), eg375@cam.ac.uk (E.I. Galindo-Nava).

https://doi.org/10.1016/j.actamat.2020.05.007

embrittlement. However, most studies have tended to focus on specific alloys, their diffusion properties and the severity of HE under particular service conditions [9–12]. The effect of microstructure has received less attention in comparison – while there are still a number of studies on the topic, they are fewer and often not particularly quantitative. They either present a limited characterisation of the microstructures studied or focus on the effect of only one particular microstructural constituent while disregarding the concurrent effect of the rest [5,13,14]. While this is understandable given the complexity of martensitic steels, it is nevertheless necessary to quantify all types of defects present to gain a complete understanding of their effect on H diffusion and embrittlement. Avoiding the complicating effect of transition metal carbides and focusing only on near-binary Fe-C martensites, dislocations, grain boundaries (GBs), retained austenite (RA) and vacancies can all have a significant effect on H diffusion. This is due to high dislocation density, small effective grain size due to the presence of martensitic subunits, and the fact that H diffusion properties of austenite are very different from martensite/ferrite, respectively. All three types of defects have been investigated, although we have found no studies attempting to deconvolve their effect in a systematic manner.

In an early study, Sakamoto and Mantani [15] tempered quenched Fe-C-Si-Mn steels of various C contents at different temperatures. They found that H diffusivity is inversely proportional to the C content and increases with tempering temperature. They ascribed the reduction in diffusivity at lower temperatures to a combination of higher dislocation and vacancy density but did not investigate the contributions from individual defects. Wei and Tsuzaki [13] investigated the effect of tempering temperature on H diffusion in a 0.2C Fe-C steel by means of thermal desorption. They found that the concentration of trapped H steadily decreased with increasing tempering temperature with a small increase near 650 °C. They suggested that this was a result of simultaneous recovery and recrystallisation which temporarily increases the trap density before grain growth reduces it again at higher temperatures – while this mechanism seems plausible, the observed increase in absorption was low and could well have been attributed to experimental scatter. Chan et al. [16] performed a thorough study of the effect of RA. They investigated a range of as-quenched martensitic steels with different C concentrations and correspondingly different RA volume fractions measured by XRD while keeping the grain size constant. They measured their H diffusivity and the H concentration after cathodic charging. They also compared the as-quenched conditions to cryogenically treated conditions with reduced RA content. Their results showed that cryogenic treatment reduced the H concentration after charging relative to the microstructures that were only quenched, implying this was due to the loss of RA, although its volume fraction before and after the cryogenic treatment was not compared. Their conclusion was that H is trapped at the RA interface and has a high associated binding energy. While the grain size in all their samples was the same, the dislocation density was not measured and its impact on diffusion therefore not evaluated. Dislocation density likely varied appreciably due to the varying carbon content of the steels [17]. Mine et al. [18,19] studied near-pure ferritic iron heavily deformed by high-pressure torsion. While not martensitic, the microstructures had a dislocation density on the order of 10^{15} m^{-2} and a grain size of 100 nm - values sufficiently close to most martensitic steels. No austenite was present and the dislocation density was measured using the Williamson-Hall method. They showed that both GBs as well as dislocations have a significant impact on H diffusion. Yang *et. al.* [19] looked at the effect of varying grain size while keeping the RA volume fraction constant. They found a notable decrease in diffusivity by decreasing the prior austenite grain size from 29μm to 8μm in tempered martensite without RA. The reduction in grain size only led to a small reduction in diffusivity when RA was present, showing that the latter had a much stronger impact on H diffusion.

While the studies reviewed above attempt to isolate the effect of individual defect types in martensite on H diffusion, they are based on a somewhat incomplete characterisation of the materials investigated. In particular, dislocation density is either not addressed or is calculated with the Williamson-Hall method, which has been shown to be inadequate for characterising martensitic steels [20,21]. It is a crucial missing piece of the puzzle given that it is expected to have a significant effect on H diffusion and that it scales with the carbon content [17], which varied in some of the studies cited. In this work we examine the H diffusion properties of several lath-martensitic microstructures by means of thermal desorption analysis (TDA) and electrochemical permeation. The microstructures are characterised more thoroughly than in the existing literature, including the grain size, RA volume fraction and dislocation density. These microstructural parameters are then used as a basis for H diffusion modelling, which serves as a tool to estimate the relative effect of each of the three defect types on H diffusion. Discussion and analysis is presented on why RA cannot be effectively treated as a point trap and why it needs to be accounted for at the very least in 2D.

2. Material and methods

The material used to produce model martensitic microstructures was DP800, received in the form of 1.5 mm thick cold-rolled and zinc-plated sheets. Its composition is shown in Table 1.

To prepare permeation, thermal desorption, and synchrotron samples, the material was cut into 8-by-4 cm plates which were wrapped in stainless foil and solutionised in a furnace for 15 min at 1100 °C. All were directly quenched into ice water, after which two sets of samples were tempered for one hour – one at 300 °C and the other 450 °C. These microstructures are referred to as AQ (as-quenched), 300T and 450T, respectively. The permeation samples were ground on an automatic grinder down in two different batches to a thickness of 821 ± 14 μm and 699 ± 10 μm, respectively. The samples were ground from both sides evenly and given a 1200 grit finish. Note that all the grinding routes completely removed the Zn-plated layer. To make synchrotron XRD samples, sticks with a square cross-section with a side length of ~0.7 mm were cut widthwise from these plates for each of the three conditions. For the thermal desorption samples, the heat-treated plates were cut into smaller 4 cm-by-1.5cm pieces and given a 1200 grit finish, retaining an average thickness of 1.425 ± 0.01 mm.

2.1. Synchrotron XRD

The experiments were carried out at the beamline I11 of the Diamond Light Source, Oxford, whose characteristics are described in detail in [22]. The energy of the incoming radiation was 15 keV and the scans lasted 45 min at a step size of 0.001°.

2.1.1. Dislocation density determination

The dislocation density was evaluated with the convolutional multiple whole profile CMWP analysis procedure [21,23,24]. The

Table 1
Chemical composition of DP800-GI in wt%.

C	Si	Mn	P	S	Al	N	Nb	V	Ti	B	Ca	Fe
0.127	0.260	2.054	0.014	0.001	0.036	0.0041	0.001	0.007	0.016	0.0002	0.0026	bal.

method is based on physically well-established profile functions of strain, size and planar-fault broadening of diffraction peaks. Strain anisotropy is handled by the use of dislocation contrast factors. The strain profile function is given by the mean square strain $\langle \epsilon^2_{g,L} \rangle$ in the Fourier transform of strain profiles [25], where $\langle \epsilon^2_{g,L} \rangle$ is given by the Krivoglaz–Wilkens theory for dislocated crystals [26,27]

$$\langle \epsilon^2_{g,L} \rangle \approx \frac{\rho \overline{C} b^2}{4\pi} f(\eta) \tag{1}$$

where g is the length of the diffraction vector, L is the Fourier variable, ρ and b are the density and the Burgers vector of dislocations, $\overline{C}$ is the average dislocation contrast factor and $f(\eta)$ is the strain function. $f(\eta)$ describes the L-dependence of the mean-square-strain with $\eta = L/R_e$, where R_e is the effective outer cut-off radius of dislocations. The dislocation contrast factors can be averaged over the permutations of indices hkl if the sample is polycrystalline or if all possible Burgers vectors are activated. For cubic crystals the average contrast factor can be given as

$$\overline{C} = \overline{C}_{h00}(1 - qH^2) \tag{2}$$

where $\overline{C}_{h00}$ is the average contrast factor of the $h00$ reflections and $H^2 = (h^2k^2 + h^2l^2 + k^2l^2)/(h^2 + k^2 + l^2)^2$. The parameter q depends on the elastic constants of the crystal and the edge or screw type of dislocations, and can be evaluated numerically [21,28]. Apart from the dislocation density, the technique also yields an error estimate, derived from the difference of the fitted profiles and experimental data points.

2.1.2. Austenite volume fraction measurement

For the calculation of austenite volume fraction the XRD patterns were fitted in HighScore+ software using pseudo-Voigt functions to fit individual peaks. Dickson's method was then used to derive the austenite volume fraction [29]. It was developed specifically for this purpose in the case of near-binary mixtures of austenite and ferrite/martensite. The method was used as an alternative to the more commonly used Rietveld refinement method because it is straightforward to apply in the case of heavily textured samples such as those studied here. The volume fraction ratio is defined as

$$\frac{v_{f\gamma}}{v_{f\alpha}} = \frac{n_\alpha}{n_\gamma} \frac{\sum_{i=1}^{n_\gamma} \frac{I_{i\gamma}}{R_{i\gamma}}}{\sum_{j=1}^{n_\alpha} \frac{I_{j\alpha}}{R_{j\alpha}}} \tag{3}$$

where v_f, I_i and n stand for volume fraction, integrated peak intensity of peak i and number of measured peaks, respectively. The indices γ and α stand for austenite and ferrite, respectively, while R stands for the theoretical peak intensity and is a product of the scattering factors of the unit cell, peak multiplicity, temperature, absorption and the Lorentz-polarisation factor [30].

The ratio will tend to converge to a constant value as n approaches infinity, although in practice only several peaks are needed for satisfactory convergence. This is convenient as it is experimentally difficult to obtain more than a few austenite peaks that are distinguishable from the background noise when the volume fraction of austenite is on the order of a few percent. Because of this, only the range between 20° and 55° was used for the calculation of the volume fraction of austenite.

2.2. Microscopy

Optical microscopy of the as-quenched microstrucure was performed to measure the size of prior austenite grains (PAG). The material was embedded into bakelite and ground to a 4000 grit finish, after which the sample was rinsed with deionised water and immediately dipped into Marshall's reagent, composed of a solution of 8 g of oxalic acid and 5 ml of 95% H_2SO_4 in 100 ml water, mixed with 100 ml of 35% H_2O_2. The sample was etched for 10 s to 15 s and imaged on an Olympus BH microscope using a Leica DFC295 camera.

TEM was performed on all three microstructures. To make the TEM samples, the material was cut into small plates, ground down to 100-150 μm and small disks 3 mm in diameter were punched out of the plates. The disks were then ground further to a final thickness of 50 μm and electropolished in a solution consisting of 70% ethanol, 25% glycerol and 5% perchloric acid by volume using a Struers Tenu-Pol-5 electropolisher. The imaging of the tempered microstructures was performed on a Tecnai F20 transmission electron microscope while the as-quenched condition was imaged on a Tecnai Osiris 80–200, both at 200 keV. Principal component analysis (PCA) using HyperSpy [31] was performed on the STEM EDX datasets to denoise the spectra. HyperSpy is an open source analysis tool-kit, where multivariate statistical analysis algorithms are implemented. PCA can be used for noise reduction in chemical maps and identification of structural features with specific chemical compositions – the details of the method can be found in the literature, e.g. [32].

2.3. Electrochemical permeation

Hydrogen permeation experiments were carried out using the standard Devanathan-Starchurski double cell kept at a constant temperature of 30 °C. The oxidation (exit) side of the cell (800 ml) was filled with nitrogen-deaerated 0.1 M NaOH and a polarisation of 200 mV *vs* a Hg/HgO reference electrode was applied. This was sufficiently low to ensure H oxidation at the exit surface was not rate-limiting. A passivation background current lower than 10^{-3} A m^{-2} was attained after 18 h of anodic polarisation to prepare the H exit surface for the oxidation of permeating hydrogen. To achieve permeation, a constant current density of 0.22 A m^{-2} was applied to the reduction (entry) side of the cell. A solution of 1 M NaCl, adjusted to pH 9 to avoid spurious surface reactions on the entry side sometimes observed in NaCl solutions using 0.1 M NaOH, was deaerated for a period of 18 h (to an oxygen concentration of < 50 wppb) using high-purity nitrogen in a 5 l aspirator during the acquisition of the oxidation background current. This continuously deaerated charging solution was then circulated to the charging side of the cell and the cathodic current was applied. A saturated calomel electrode was used as the reference electrode for the charging cell and a Cl-free, Hg/HgO reference electrode was used on the exit side in order to avoid crevice corrosion. Graphite counter electrodes were used on both sides and all the measurements were conducted on a PAR multistat in floating mode.

Two sets of experiments were performed, one on a thinner batch of samples, one on a thicker batch with the average values of 821 ± 14 μm and 699 ± 10 μm respectively. This was to ensure reproducibility and that the diffusion trends were independent of the sample thickness and that the data gathered showed that diffusion through the samples – and not surface reactions – was the rate-limiting step. To obtain the average thickness values, five measurements were taken per sample with a micrometer – four measurements around the perimeter and one from the centre of the permeation area of the samples.

For the evaulation of the permeation data, the time lag was defined as the time t_t at which the permeation current reaches 63% of the steady-state value. Time lag was used to extract the effective H diffusivity D_{eff}, respectively, as [33]

$$D_{eff} = \frac{l^2}{6t_t} \tag{4}$$

where l is the thickness of the sample. Time lag was also used to evaluate H trap site density N_t from the following equations for strong (*i.e.* near saturation) and weak traps, respectively [34]

$$t_t = \frac{l^2}{6D_l}\left(1 + \frac{3N_t}{c_{l,BC}}\right) \tag{5}$$

$$t_t = \frac{l^2}{6D_l}\left(1 + \frac{N_t}{N_l}\exp\left(\frac{\Delta E_t}{RT}\right)\right) \tag{6}$$

where D_l is the lattice diffusivity of pure iron taken as 4.2×10^{-8} exp $(-3850/R/T)$ m^2 s^{-1} [35], N_l is the density of interstitial sites in the lattice that may accommodate H atoms, $c_{l,BC}$ is the H lattice concentration at the entry surface and ΔE_t is the binding energy of the trap. Eqs. (5) and (6) are limiting cases of a more general analytical solution of the McNabb-Foster diffusion model derived elsewhere [36].

2.4. Hydrogen charging and thermal desorption

The solution of 3 wt% NaCl and 3 g l^{-1} NH_4SCN in deionised water was used, following Akiyama and Li [37]. By conducting a series of galvanostatic permeation experiments they mapped the corresponding steady-state permeation current from which the boundary condition for H charging can be derived with the following equation

$$i_\infty = FD_l\frac{c_{l,BC}}{l} \tag{7}$$

where i_∞ is the steady-state permeation current and F is the Faraday constant. It is simply Fick's first law under the assumptions of a linear concentration gradient and null concentration on the exit side. The concentration and the diffusion coefficient from Eq. (7) are sometimes interpreted in the literature as the total H concentration (including traps) and the effective diffusion coefficient, respectively. Given that trapping effects are transient and that Eq. (7) assumes steady-state diffusion, this interpretation should be avoided. Note also that while the diffusion coefficient in the equation is that of the lattice when dealing with ferrite/martensite where GBs and other defects are not fast pathways for H diffusion [38], this may not be true of some FCC alloys, such as Ni alloys. There, the grain size should be sufficiently large to eliminate the effect of GB diffusion [39].

Thermal desorption samples were spot-welded onto a stainless steel wire. The plate edges and the wire itself were coated with a layer of non-conducting varnish to restrict H ingress to plate faces. The charging was performed in 150 ml of the above solution with a Gamry Interface 1000E galvanostat under a current density of 0.3 mA cm^{-2} for 24 h using a platinum coil counter electrode. The current density and charging duration were sufficient to fully saturate the samples. After charging, they were rinsed with deionised water and immediately stored in liquid nitrogen to prevent hydrogen effusion. TDA was performed in an Agilent 7890B gas chromatograph – the samples were removed from liquid nitrogen and given an ultrasonic acetone bath for 1 min. They were transferred to the rig which was purged for 20 min before the start of the experiment. The heating rate used for all experiments was 100 °C h^{-1}.

2.5. Diffusion modelling

The multi-trap diffusion model used here was described in previous studies [8,39]. Note that in the diffusion equation there the trapping term on the right hand side was erroneously missing the trapping factor K_t in the numerator. The diffusion equation reads

$$\frac{\partial c_l}{\partial t} = \left(1+\sum_{k=1}^{m}\frac{V_l}{V_{tk}}\frac{K_{tk}}{\left(K_{tk}+V_l c_l(1-K_{tk})\right)^2}\right)^{-1} \left(\frac{\partial}{\partial x}\left(D_l\frac{\partial c_l}{\partial x}\right)-\sum_{k=1}^{m}\left(\frac{1}{V_{tk}}\frac{c_l^2V_l^2-c_lV_l}{\left(K_{tk}+V_lc_l(1-K_{tk})\right)^2}\frac{K_{tk}\Delta E_{tk}\phi}{RT^2}\right)\right) \tag{8}$$

where lattice and trap site density N_l and N_t have been substituted with their inverses V_l and V_t for clarity. Index k stands for the type of trap, ΔE_{tk} is the trap binding energy, K_{tk} is its equilibrium constant defined below, T is the temperature and ϕ is the heating rate. The basis for this model is the notion that the total hydrogen concentration can be split into lattice hydrogen c_l and hydrogen bound to trap k, c_{tk} and that the two populations are in thermodynamic equilibrium [40]

$$c_{tk} = \frac{V_l}{V_{tk}}\frac{1}{K_{tk}+V_lc_l(1-K_{tk})}c_l;\ \ K_{tk} = \exp\left(\frac{-\Delta E_{tk}}{RT}\right) \tag{9}$$

This allows expressing the time derivative of the ordinary diffusion equation as a sum of c_l and c_{tk} time derivatives. Using Eq. (9), the derivatives can be recast in terms of c_l and trapping parameters. The spatial derivatives of concentration remain the same under the assumption that traps are not hydrogen diffusion paths – the total concentration in this term can thus be substituted for c_l. The second sum term in Eq. (8) comes from taking the total rather than partial time derivative of c_{tk}, as both K_{tk} and T are time-dependent in TDA. The first term on the right-hand side of the first line of Eq. (8) represents the reduction diffusivity due to the effect of traps, while the last sum term on the second line represents the change in the equilibrium between H in lattice and trap sites due to temperature. Note that in the formulation upon which Eq. (8) is built [41] allows the possibility of H diffusing along trapping sites as done in a previous study of grain boundary diffusion effects in an austenitic steel [39]. This may also be of some relevance in martensite where defects such as dislocations and grain boundaries are arranged in a hierarchical way as lath boundaries and various other subunit boundaries. If future atomistic studies reveal that H diffusivity along these structures is significantly different from the lattice, the analysis from this study is worth revisiting. However, current literature suggests that in BCC iron that is not the case either for grain boundaries or dislocation cores [38,42]. We can therefore assume that the structured arrangements of subunit boundaries and dislocations in martensite can be approximated as point traps reasonably well, which is the approach used in this study. The effect of regions of material with different H diffusivity is examined in part II of this series where we focus on the effect of retained austenite morphology. The strategy we applied to modelling the effect of austenite could in principle also be applied to studying H diffusion along defect structures in martensite.

Eq. (8) was implemented as a finite difference scheme in Matlab and was used to simulate the experimental permeation and thermal desorption experiments. The boundary condition assumptions for permeation were a constant value on the ingress side derived from the experimental value of the steady state current and a constant zero concentration on the exit side assuming rapid H oxidation kinetics. Note that in the experiments the current density, the potential and the ph at the ingress side did not vary throughout the duration of the experiments, giving additional confidence to the boundary condition assumption of a constant H concentration. For thermal desorption, the simulation steps were similar, except that the charging step was simplified by assuming uniform initial c_l equal to the charging boundary condition. The time elapsed between the charging and thermal desorption steps was 1200 s, the same as in experiments. Up to three trapping terms were considered, corresponding to dislocations, GBs and RA.

3. Experimental results

3.1. Synchrotron XRD – fraction of retained austenite and calculation of dislocation density

The patterns obtained showed significant texture, likely due to the rolling process used in the manufacturing of the material. They also lacked any traces of peak splitting associated with a tetragonal BCC unit cell characteristic of higher-carbon martensite. This was expected since tetragonality in martensite is known to be appreciable only when the carbon concentration exceeds 0.18 wt% C [43]. The binned raw data along with the fits obtained with the dislocation density model are shown in Fig. 1. Fig. 1b–d show the patterns and

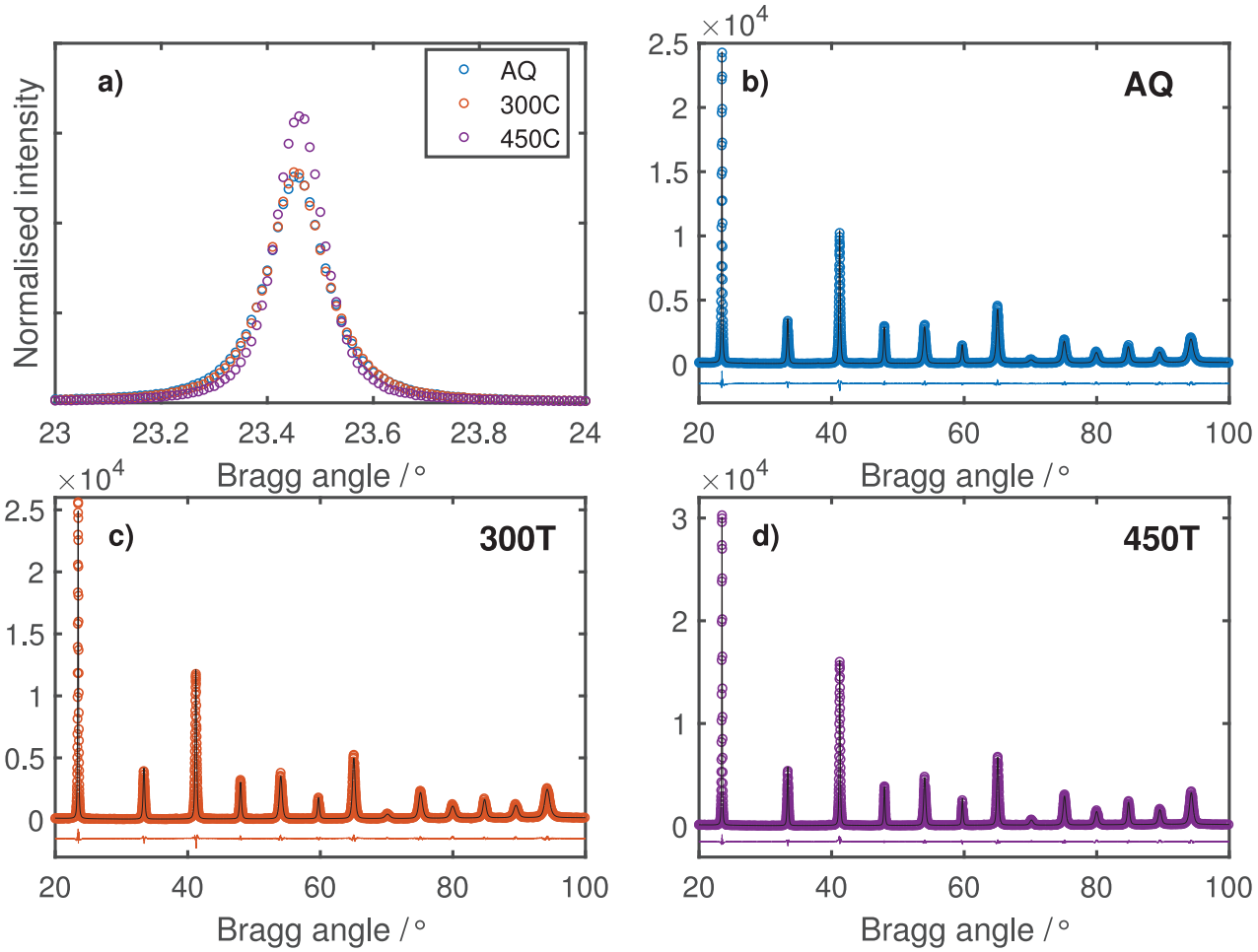

Fig. 1. a) comparison of the first martensite peak between the three microstructures normalised by peak area. b), c) and d) XRD patterns and the fits used for the determination of dislocation density. The circles are experimental data points, the black lines show the model fits while the coloured lines at the bottom show the difference between the two. The y-axis units in b-d) are detector counts. Martensite peak indices are (110), (200), (211), (220), (310), (222), (321), (400), (330), (420), (332), (422) and (431) at positions 23.4, 33.4, 41.2, 47.9, 54.0, 59.7, 65.0, 70.0, 75.0, 79.9, 84.7, 89.4 and 94.1, respectively.

the fits from the procedure for the calculation of dislocation density. Fig. 1a shows that the peak shapes of the AQ and 300T samples are nearly identical, indicating that the dislocation density and crystallite size values are very similar. The 450T peak, however, is noticeably sharper, indicating a lower associated dislocation density.

To obtain the volume fraction of austenite, the XRD patterns were binned such as to keep approximately 10 data points above the full width at half maximum of the narrowest peak, i.e. peak 1. The data were then truncated, taking only the range from 22° to 50° as this is where the austenite peaks are still discernible. The XRD profiles were then fitted in HighScore+ software using a background polynomial and pseudo-Voigt functions to fit individual peak profiles. The areas of ferrite and austenite peaks obtained this way were used in Dickson's method to derive the volume fraction of austenite. Using values of the first four ferrite and the first four austenite peaks, the austenite volume obtained was 3.5 ± 0.6 vol.%. Rietveld refinement was also attempted, but led to relatively poor pattern fits due to the presence of strong texture, despite using the March-Dolasse factors that are supposed to account for these effects. Regardless, the obtained austenite volume via Rietveld refinement was around 3 vol.% – similar to that obtained via Dickson's method, providing further confidence in the value obtained.

The values of RA volume fraction and the dislocation density are collected in Table 2. The dislocation densities in the AQ and 300T samples are very close, while the density in the 450T sample is notably lower, by about a factor of 2.5.

Table 2
Density of dislocations and volume fraction of RA in the investigated samples.

Sample	RA /vol.%	$\rho/10^{15}$ m^{-2}
AQ	3.5 ± 0.6	8.6 ± 1.0
300T	~0	7.4 ± 1.0
450T	~0	3.3 ± 0.4

3.2. Microscopy

Fig. 2 a shows one of the optical micrographs used to measure the average PAG size. A total of 39 grains in two images were manually outlined with the polygon tool in ImageJ, as illustrated in Fig. 2b. Assuming circular shape, their average area was converted to average diameter with a final value of 25.8 ± 0.4 μm. This value was used as input for permeation simulations.

To examine the presence of carbides, cementite and RA, bright field (BF) TEM was performed on all three conditions and the results are displayed in Fig. 2c–e. The martensitic microstructure does not appear to change much between conditions, apart from some cementite coarsening, particularly in the 450T case. However, the AQ condition should contain films of austenite based on the XRD analysis, while the tempered conditions should be austenite-free. Sparse Ti-V-based carbides of blocky morphology could also be detected in all three conditions.

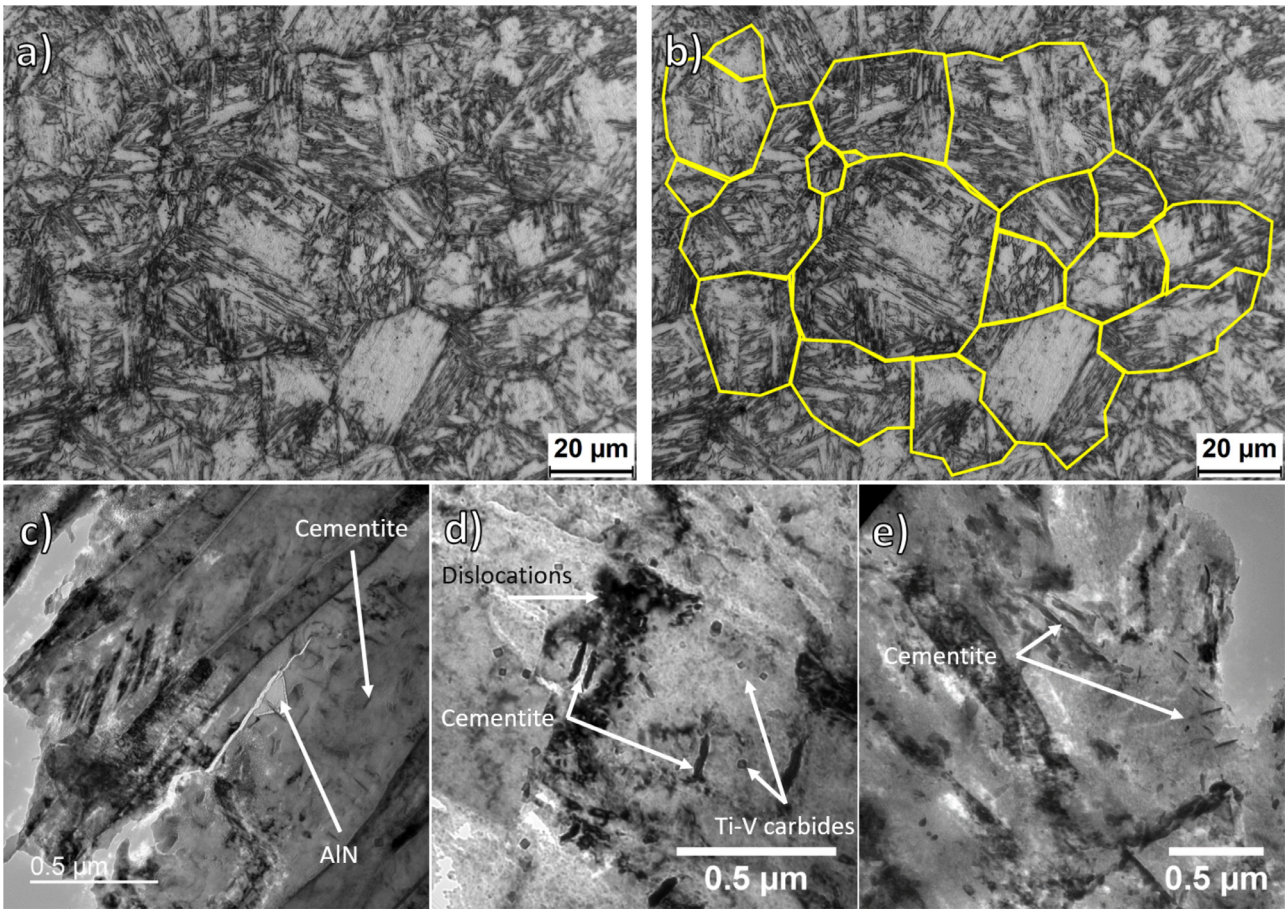

Fig. 2. a) Optical micrograph of the as-quenched (AQ) microstructure etched to reveal prior austenite GBs. b) Example of the grain size measurement procedure. c)-e) BF TEM micrographs of the three microstructures, AQ, 300T and 450T, respectively.

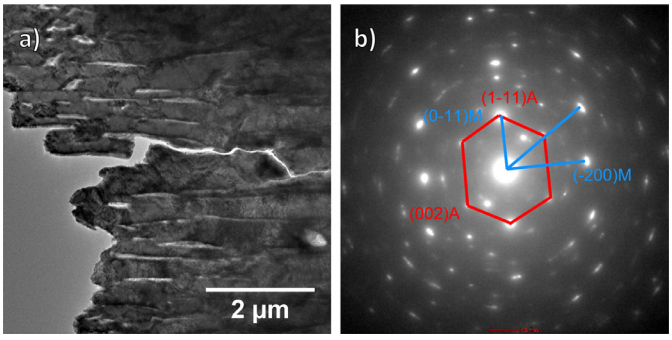

Fig. 3. a) TEM image of the AQ microstructure showing austenite films; b) the corresponding diffraction pattern with overlapping martensite and austenite reflections both with the zone axis [110].

Austenite was identified in the AQ sample in diffraction mode from the bottom right area shown in Fig. 3a. A diffraction pattern shown in Fig. 3b clearly contains two distinct patterns, identified as the reflections of martensite and austenite.

Additional STEM-EDX mapping was performed on the AQ condition to identify the carbide composition and the results after PCA are shown in Fig. 4. Most mapped precipitates appear to be cementite, while a few are Ti-V-based carbonitrides. There is a noticeable nitrogen content in all the precipitates scanned. Assuming that the samples have an isotropic precipitate distribution and assuming that the EDX spectra represent a two-dimensional section of the microstructure, 6 particles per 500^2 nm^2 yield a number density of $\sim 10^{20}$ m^{-3}. Note that this is an overestimate as other areas of the AQ sample scanned by STEM-EDX showed much lower carbide counts and were often even carbide-free. The resulting H trap density, estimating the average diameter to be $\sim$ 10 nm is on the order of 5 mol^{-3} based on a scaling law from [8], which is low given their relatively weak binding energy ($\sim$35 kJ mol^{-1} [8]). We can conclude that their effect on the overall diffusion behaviour is therefore negligible given the high density of other defects.

STEM-EDX and PCA were also performed on lath boundaries, where the presence of RA was expected to be linked to elemental segregation, particularly of carbon. Fig. 4b shows that is indeed the case as one of the primary components derived from PCA shows

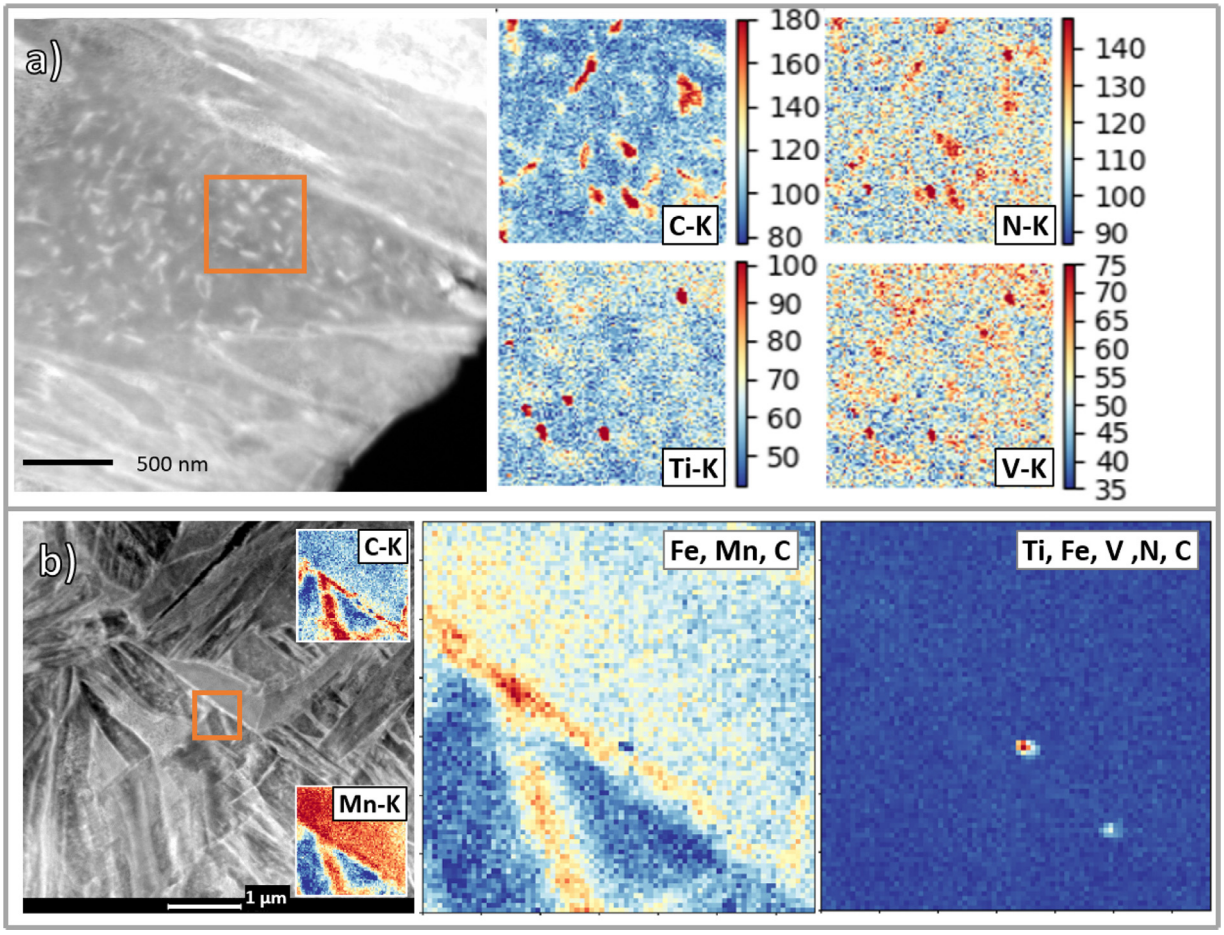

Fig. 4. a) Drift-corrected HAADF STEM image of a carbide-rich area of the AQ microstructure. The orange box represents the area of the EDX scan. In the EDX maps on the right some of the precipitates are clearly cementite while others are Ti-V-based carbonitrides. The scale bars represent the number of detector counts within the energy window defined for the K peaks of the elements shown. b) Drift-corrected HAADF STEM image of the AQ microstructure showing numerous laths. The insets are the are PCA-denoised signals of C and Mn K_α radiation. Next to it are images of the two principal components resulting from PCA, the first of which is associated to signals of Fe, Mn and C and the second of which is associated to Fe and carbide-forming elements.

that the boundary is enriched in C and Mn which normally segregate to austenite. This is also evident from denoised EDX maps of C and Mn, shown as insets. While C is located exclusively at interfaces, the Mn signal, while strongest at the interface, is also strong in the top part of the image. This likely results from the greater thickness of the sample.

3.3. *Permeation and thermal desorption – experimental*

Fig. 5 shows the permeation and thermal desorption results. In permeation, both batches (Fig. 5a–c) show very similar behaviour, highlighting the reproducibility of the experiments. The small variations observed are likely a result of differences in sample thickness and slight variations in charging conditions. The AQ samples in Fig. 5a show a dramatic increase in time lag compared to the tempered samples.

A number of trapping parameters were estimated from the permeation curves and are listed in Table 3. Eqs. (4)–(6) were used to extract the effective diffusivity D_{eff}, the density of strong traps and the density of weak traps, respectively. For the lattice diffusivity D_{l} of ferrite, the relationship $4.2 \times 10^{-8} \exp(-3850/R/T)$ $\mathrm{m^2\ s^{-1}}$ was used [35], yielding 9.1×10^{-9} $\mathrm{m^2\ s^{-1}}$ at 30 °C. The steady state permeation current i_∞ and as a consequence the H lattice concentration at the ingress surface $c_{\mathrm{l,BC}}$ are very low in all cases. This is partly due to the fact that no H recombination poisons were used on the entry side; in addition, NaCl solutions intrinsically seem to produce lower surface concentrations compared to e.g. NaOH or H_2SO_4 [44–46]. Note also that plating the oxidation side of the sample with Pd, common in the literature, also increases the steady state current [47], but was not done in our case to prevent H entry which takes place during electrochemical plating. More importantly, however, the $c_{\mathrm{l,BC}}$ values are reasonably consistent, as expected from the theory and given the tight control over the experimental parameters. The values are used in the next sections for the modelling of permeation curves.

Based on the permeation data and microstructural characterisation, the 300T and 450T conditions were expected to contain similar trap densities of relatively weak traps, while the AQ condition should in addition contain a low density of strong traps that cause the permeation transient rise to stay steep while increasing the time lag dramatically. Why only the presence of strong traps can explain the permeation transients of the AQ samples is discussed later.

Fig. 5 d–f show the thermal desorption curves of the three microstructures. The experiments were repeated up to three times per condition to evaluate the scatter, which was negligible for the 450T samples but more evident for the 300T and AQ ones. The average total H concentrations of 1.23 ± 0.07 wppm,[1] 0.79 ± 0.09 wppm and 0.56 ± 0.01 wppm, for AQ, 300T and 450T samples, respectively. This is in line with the trends observed in permeation – the AQ microstructure evidently

[1] The conversion factor from wppm to mol $\mathrm{m^{-3}}$ is 7.84 mol $\mathrm{m^{-3}}$ $\mathrm{wppm^{-1}}$.

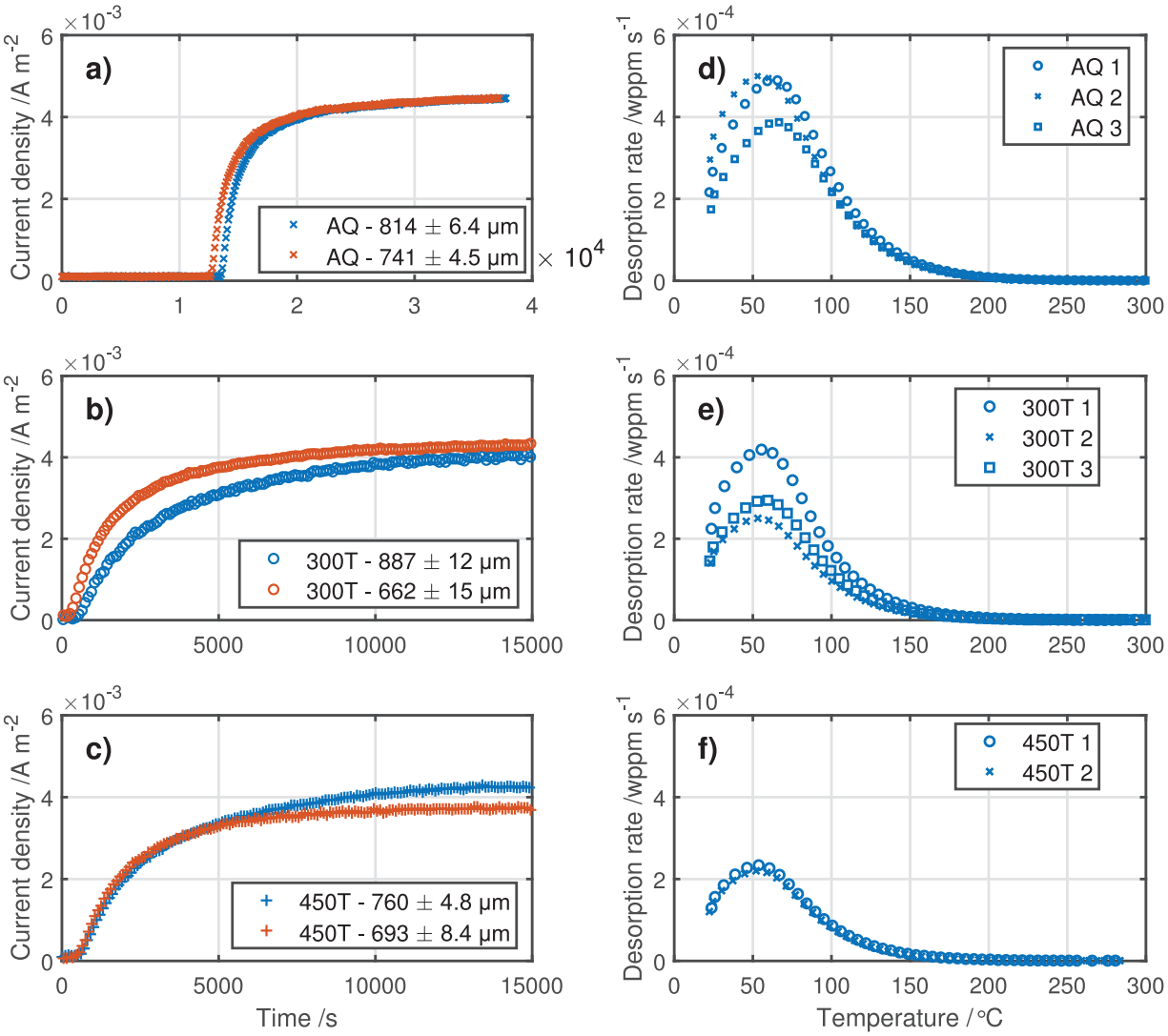

Fig. 5. Permeation curves from three microstructures in a-c) and the corresponding thermal desorption curves in d-f). The average H concentrations measured in TDA were 1.23 ± 0.07 wppm, 0.79 ± 0.09 wppm and 0.56 ± 0.01 wppm for the AQ, 300T and 450T conditions, respectively.

Table 3
Parameters extracted from permeation experiments using Eqs. (5) and (6). * signifies strong traps (Eq. (5)) which are expected only in the AQ samples, while ** signifies weak traps (Eq. (6)) (assumed 30 kJ mol^{-1}) which are present in both but have a lower impact compared to the strong traps in the AQ samples.

Parameter		Thick samples			Thin samples		
		AQ	300T	450T	AQ	300T	450T
i_∞	/10^{-3} A m^{-2}	4.36	4.09	4.15	4.32	4.28	3.68
$c_{l,BC}$	/10^{-3} mol m^{-3}	4.10	4.19	3.64	3.70	3.28	2.95
t_t	/10^{3} s	15.6	3.25	3.20	13.7	2.15	2.25
D_{eff}	/10^{-12} m^2 s^{-1}	7.08	40.3	30.1	6.68	34.0	35.5
N_t*	/10^{-3} mol m^{-3}	1.76	–	–	1.86	–	–
N_t**	/mol m^{-3}	–	309	415	–	367	350

contains additional traps and therefore absorbs more H than the other two. Permeation results suggest that 300T and 450T have similar H trapping properties. While thermal desorption data show that the 300T samples trap more H than 450T, the difference is small and is likely a result of the difference in dislocation densities between the two conditions as shown by synchrotron XRD peak analysis and as further discussed in the next section.

3.3.1. Quantification of trapping parameters

Before attempting to model thermal desorption and permeation, the effect of the main microstructural constituents – dislocations, GBs, RA, cementite and possibly vacancies – must be evaluated and deconvolved. The binding energy ΔE_t and trap density N_t for each defect type need to be found in order to perform any meaningful modelling. The analysis of the permeation transients are shown in Table 3. A slight discrepancy to note is the lower measured D_{eff} value of the thick 450T sample compared to the 300T sample. Because the former was tempered at a higher temperature, a somewhat lower trap density and therefore higher D_{eff} value would have been expected. This discrepancy can be due to experimental error or uncertainty in sample thickness. It could also be due to a higher initial dislocation density of the 450T sample; either due to a higher cooling rate during quenching or a different thickness of the surface layer removed by grinding during sample preparation. The table lists rough estimates of N_t assuming some range of ΔE_t values. However, it only yields an average value which is not applicable to systems with multiple distinct traps. We therefore perform a parametric analysis of the diffusion model in Eq. (8) to examine the effect of ΔE_t and N_t on the shape of permeation transients as it will be helpful in discussing the relative contributions of different defects to H permeation behaviour.

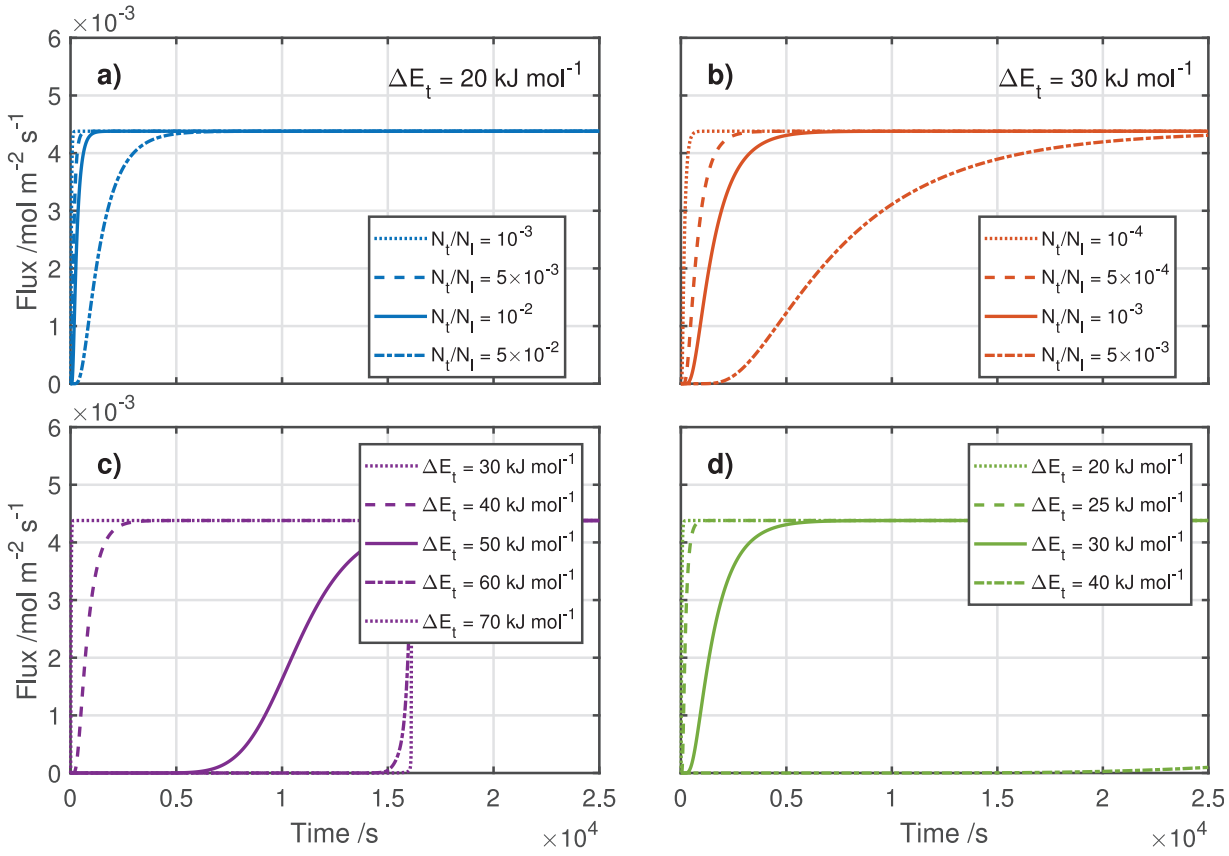

Fig. 6. Illustration of the effect of ΔE_t and N_t on the shape of permeation curves. The boundary condition applied on the ingress side was 3.7×10^{-3} mol m^{-3}, similar to the values obtained from experiments. The thickness used was 741 μm and the D_l was 8.97×10^{-9} m^2 s^{-1}. a) and b) show the effect of N_t at ΔE_t 20 kJ mol^{-1} and 30 kJ mol^{-1}, respectively. c) and d) show the effect of ΔE_t at the N_t/N_l ratio of 10^{-5} and 10^{-3}, respectively.

Fig. 6 highlights the effect of these trapping parameters. Two features are worth noting – while both ΔE_t and N_t affect the permeation time lag and breakthrough time, increasing N_t always results in a slower, shallower rise. On the other hand, increasing ΔE_t initially has the same effect but increasing it further leads to a progressively steeper curve as shown in Fig. 6c. This stems from the fact that strong traps absorb a large fraction of lattice hydrogen at every time step. As a result, the H lattice concentration will be extremely low in the regions where traps have not yet reached saturation while staying relatively high in the regions where traps have already saturated. This leads to high gradients in c_l where these two regions meet, which results in a much higher rise in permeation flux compared to the case of weak trapping where the gradients in c_l are not as large.

This effect on the steepness of the transient is important as it implies that to have both a large time lag and a steep transient, as experimentally observed in the AQ microstructure, a high binding energy ΔE_t is needed. The second feature is that at low ΔE_t, the trap density needs to be extremely high to result in any significant time lag. For example, in Fig. 6a the N_t/N_l ratio of 5×10^{-2} means a N_t value of $\sim 10^4$ mol m^{-3} produces a time lag of only a few hundred seconds taking the value of N_l as 2.04×10^5 mol m^{-3} [41].

Let us now discuss the microstructural differences between the conditions and their implications for H diffusion. All the microstructures studied have a high effective surface area associated with martensite subunits which is constant across all samples as the tempering temperature for 300T and 450T samples was insufficient to cause recrystallisation. The trap density due to GBs is therefore also expected to be the same in all the microstructure. Furthermore, the size of martensite subunits, i.e. packets and blocks, is a simple function of the PAG size [17]

$$\begin{aligned} d_{\text{pack}} &= 0.4 d_{\text{PAG}} \\ d_{\text{block}} &= 0.067 d_{\text{PAG}} \end{aligned} \tag{10}$$

where d_{pack} and d_{block} are packet and block diameters, respectively.

The trap density due to packet and block boundaries can be derived by dividing the number of H trapping sites at the GB with the average grain volume. Note that the smallest martensite subunits, laths, are defined by low angle GBs which are essentially dislocation walls [17] – these sites will therefore be treated as dislocations. The number of trapping sites at the GB is obtained on the assumption of one trapping site per every Burgers vector squared (DFT calculations show that this is a good approximation [48]) which is divided by a factor of 2 since every GB is shared by two grains and multiplied by the average surface area of a grain. The resulting number of trapping sites per grain is divided by the average grain volume to yield

$$N_{\text{pack}} = \frac{3}{d_{\text{pack}} b^2 N_A}; \quad N_{\text{block}} = \frac{3}{d_{\text{block}} b^2 N_A} \tag{11}$$

where N_A is the Avogadro constant and b is the magnitude of the Burgers vector, taken as 2.5×10^{-10} m. Next, the ΔE_t for GBs must be identified. The values reported for GBs in ferrite vary significantly due to the limitations of TDA from which most were derived. In TDA, peaks resulting from different traps frequently overlap and it is nearly impossible to tell which defect type they are associated to. Furthermore, their position, a measure of ΔE_t, is also affected by the

sample geometry and trap density N_t – something that is rarely accounted for. Because of these limitations, ΔE_t values derived from density functional theory (DFT) are considered more reliable. Despite the fundamental nature of the DFT method however, the values of ΔE_t for different GBs vary from 30 to 45 kJ mol^{-1}, and depend not only on the GB structure but to some degree also on the simulation setup (compare e.g. [49–51]), making the choice of ΔE_t somewhat complicated. However, since Eq. (11) gives a good estimate of the trap density, we can use it to model permeation curves while adjusting the binding energy. As discussed in the next paragraphs, the effect of dislocations on the permeation curves of 300T and 450T is small and so any reduction of diffusivity relative to pure ferrite must primarily be a consequence of GB trapping. Because N_{pack} and N_{block} are known, the corresponding ΔE_t must be chosen such as to result in a good fit to the experimental permeation curves for the 300T and 450T cases where GB trapping should be the primary trapping mechanism. We assumed that ΔE_{block} and ΔE_{pack} are equal and it was found that the value of ΔE_t around 30 kJ mol^{-1} resulted in a good fit.

Next is the effect of dislocations. The trap density due to dislocations scales with dislocation density, which was measured with synchrotron XRD. However, the choice of the average N_t and ΔE_t associated to dislocations can be somewhat arbitrary since there are a number of sites with different ΔE_t values [42,52] within several Burgers vectors of the dislocation core. To tackle this, Bombač et al. [52] recently used a combination of DFT and kinetic Monte Carlo calculations to obtain equilibrium lattice and trap site concentrations in the vicinity of a single dislocation accounting for all the different sites. They fitted the values to Eq. (9) to obtain an average trapping energy. They considered all H sites to about 5 Burgers vectors from the dislocation core to be trapping sites and obtained a ΔE_t of 20 kJ mol^{-1} for screw dislocations. Their averaging procedure therefore yields both the average ΔE_t as well as N_t, leading to the following scaling law for dislocation density ρ

$$N_{dis} = N_l \pi (5b)^2 \rho \tag{12}$$

assuming that the density of H sites in the trapping region is the same as in the lattice (N_l) and that the trapping is unaffected by dislocation-dislocation interactions. Note that a similar scaling law was applied by other authors [18], but only considered trapping at dislocation cores assuming a high binding energy. Based on the arguments above, however, we consider Eq. (12) a much better approximation. At a dislocation density of 6×10^{15}m^{-2} using the average ΔE_t value of 20 kJ mol^{-1}, the N_{dis}/N_l ratio is about 3×10^{-2} which produces only a modest time lag as seen from Fig. 6a. Unlike previous studies, this suggests that dislocations have a minimal effect on H diffusion – in itself certainly not enough to explain the experimental data shown in Fig. 5. This is in line with the permeation and TDA results, where the 300T samples have ~2.5 times higher ρ values compared to the 450T ones and yet the H diffusion and trapping behaviour is very similar in both.

Finally, the presence of RA in the AQ condition must be discussed. The main question is the nature of the sites related to H trapping, whether that is primarily the bulk of the austenite islands or their interface – the literature is replete with contradicting conclusions [53–56]. It must be emphasised that bulk trapping should be possible – while H diffusivity in austenite is low, it is not as prohibitively low as in carbides. Assuming a D_l of 10^{-16} m^2 s^{-1} in austenite, a grain with a diameter of 100 nm will saturate in ~25 s. In order for the interface trapping hypothesis to hold there must be some large energy barrier associated with the transition of H from the α-γ interface into the γ bulk. There are indeed thermal desorption and permeation studies suggesting that RA islands have a high associated ΔE_t [54,57], but no DFT studies of this interface have been performed to date. The experimental results mentioned may be consistent with the interface energy barrier hypothesis, but may also result from bulk trapping and the fact that H takes a longer time to effuse because of its low diffusivity in austenite islands.

Let us assume that trapping occurs in the bulk of austenite and that the lag mentioned above is negligible and austenite can be treated with the local equilibrium approach. The energy difference ΔE_t between lattice sites in pure ferrite and pure austenite is less than 20 kJ mol^{-1} [48], making it a weak trap.[2] However, bulk trapping would have a large associated N_t – assuming it has the same interstitial site density N_l as ferrite, 3 vol.% of austenite yields a N_t of 6000 mol m^{-3}. These parameters would result in permeation transients much shallower than the ones actually observed for the AQ condition. This could mean that whatever trapping is associated with RA is linked to its interface with the matrix rather than the bulk and that the interface has a much higher associated binding energy in order to explain the sharp permeation transient. However, it is then unclear how to justify the low N_t implied from the TDA and permeation simulations discussed below, which is on the order of only 1 mol m^{-3}. Assuming that the interface traps one H atom per every Burgers vector squared, as in the case of GBs, leads to a large overestimate of N_t.

These contradictions imply that the point-trap approximation is insufficient and that bulk trapping may indeed, depending on the morphology of austenite, produce the effect observed in experiments. If the absorption kinetics are sufficiently rapid and the austenite is film-like as it generally is in low-C martensite, this seems plausible. In part II of this paper, an extension of the diffusion model to 2D is introduced along with the means of accounting for the effect of austenite explicitly and bulk trapping in austenite films is investigated further. The results there show that a fine dispersion of austenite may indeed result in a relatively large time lag and steep permeation rise – much steeper compared to a point trap with equivalent ΔE_t and N_t values – which may explain the AQ permeation curve sufficiently. Note however, that without a better understanding of its morphology, the effect of austenite can only be studied qualitatively. While austenite was indeed observed in TEM (Fig. 3), the image is unlikely to be representative of the whole microstructure and therefore cannot be taken as a sufficiently accurate input for 2D diffusion simulations. 3D imaging of RA over larger length scales would ideally be needed and is suggested as one of the avenues for potential future work.

A third possibility is that the strong sparse traps suggested by the simulations are in fact vacancies. The AQ condition was likely to have inherited some vacancies from direct quenching from a high temperature – assuming no annihilation, the atomic fraction of vacancies at the solutionising temperature of 1100 °C is in the range of 5.8×10^{-7} based on the vacancy formation energy of 164 kJ mol^{-1} [58]. This is equivalent to 0.12 mol m^{-3} and is too low on its own to explain the implied N_t. Numerous vacancies and other debris could also form during the intense plastic deformation resulting from the phase transformation to martensite. If their total concentration were indeed close to the observed N_t, they could be an explanation for the behaviour observed in the AQ microstructure – even low-temperature tempering in the case of 300T and 450T would lead to vacancies either saturating with C atoms or to their annihilation. The vacancy hypothesis, however, is difficult to test and to the best of our knowledge no quantification of vacancy concentration in martensite has been performed to date. We attempted to deconvolve the effect of vacancies and RA by immersing the AQ samples in liquid nitrogen for several days as this was expected to eliminate RA and preserve the existing vacancy concentration. XRD analysis revealed, however, that austenite peaks were still present and their intensity was unaffected. Furthermore, while the dislocation motion during the formation of martensite may generate vacancies and dislocation debris, it may also annihilate them through dislocation recombination and climb. It

[2] Only when treating it under the hypothesis of local equilibrium which only accounts for the trap density and energy difference relative to the lattice but disregards any energy barriers. Given the high activation energy for lattice diffusion of H in austenite ~ 50 kJ mol^{-1} one could argue it is a strong trap but that is beyond the local equilibrium approximation.

Table 4
Parameters used in permeation simulations.

Parameter	Value	Ref.	Comment
$c_{l,BC}$	varies	–	see Table 3
ΔE_{GB}	30 kJ mol^{-1}	–	within the range reported
ΔE_{dis}	20 kJ mol^{-1}	[52]	averaged over different trap sites near dis. core
ΔE_{RA}	55 kJ mol^{-1}		yields best steepness fit for AQ
N_{GB}	56 mol m^{-3}	Eq. (11)	sum of all grain subunits, with d_{PAG} 26 μm
N_{dis}	–	Eq. (12)	ρ values from Table 2
N_{RA}	1.7 mol m^{-3}	–	see Table 3

is therefore unclear whether the as-quenched martensite would in fact retain a high vacancy concentration.

Based on the observations and discussion so far, however, it is most likely that the large time lag and the steep permeation transient in the AQ samples are caused by RA. However, the model used here is limited to 1D and cannot describe the effect of H trapping in the bulk of austenite. It is therefore treated as a strong sparse trap site despite the problems discussed above.

Finally, the role of cementite must be discussed. Cementite has experimentally been shown to have a very low binding energy of ~15 kJ mol^{-1} [59,60] and a negligible effect on trapping – even in pearlitic steels where the effective surface area available for trapping is very high [61,62]. The same conclusion was also reached by authors who studied simple Fe-C martensitic steels – the effect of cementite was negligible regardless of the tempering temperature and the corresponding variation in morphology [13]. Its role in H trapping can therefore be neglected.

Based on the discussion above it seems reasonable that the only relevant trapping sites in the samples investigated were GBs, dislocations and RA, which were subsequently modelled under the assumption of local equilibrium as point traps with a single value of the binding energy. In reality, the H-trap interactions are likely more complicated. Just as with dislocations, GBs and various carbides also possess a number of sites with different H binding energies [50,63,63], and some average value must be taken to perform continuum-scale simulations. Since it was previously shown that trapping at dislocations can be approximated using the local equilibrium equation and a single binding energy value [52], the same approximation should be applicable to other defects. At this stage, however, similar averaging simulations have not been performed for GBs in BCC iron.

3.4. Permeation and thermal desorption – modelling

Accounting for the observations in the previous section, the permeation curves were modelled using three distinct trapping sites, dislocations, GBs and RA. All the model parameters are listed in Table 4. Note that N_t values are close to those obtained by analysing the experimental permeation curves listed in Table 3, providing additional confidence in the scaling laws proposed in Eqs. (11) and (12). Note that the density of weak traps in Table 3 is larger by a factor of ~5, which means that Eq. (11) somewhat underestimates the trap site density due to GBs, although note that in the simulations some of the time lag is due to dislocations, meaning that a lower N_t value for GBs is sensible.

A note on the choice of c_l in TDA simulations in Section 3.4: the combination of the charging solution and current density used for charging our TDA samples was investigated before in a permeation study [37] – the reason this combination was chosen was because in [37] the authors reported the steady-state current density for it. This allowed us to derive the corresponding H surface concentration to be used as the boundary condition $c_{l,BC}$ for TDA simulations. However, using the $c_{l,BC}$ value derived from [37], 0.33 mol m^{-3}, led to total H concentrations in excess of 5 wppm, much higher than in our experiments. It is not entirely clear what led to the discrepancy. The value of $c_{l,BC}$ used here was 0.082 mol m^{-3} instead.

The results of permeation simulations and their comparison to the experimental data are displayed in Fig. 7. The agreement is fairly good for the AQ and 300T conditions – any discrepancies in the time lag are within the experimental scatter. There is, however, some discrepancy beyond about $0.5i_\infty$ where the rise in i in the experimental curves slows down, while the modelled curves remain quite steep. As this effect could not be reproduced for the 300T and 450T conditions regardless of the combination of trapping parameters used, this is likely an artefact of the permeation method itself. The most likely possibilities are a decrease in oxidation kinetics on the exit side or the thickening of the local oxide film, both of which have been shown to have a significant effect on the transient [47,64]. The transients of the 450T samples are reproduced somewhat less well because of a simulated decrease in dislocation trapping due to the scaling law for N_{dis}.

We then used the same set of parameters, except c_l as discussed below, to simulate the experimental thermal desorption curves. The results are shown in Fig. 8. The trend of decreasing total H concentration from the AQ to the 300T to the 450T sample is reproduced successfully and the correspondence between the experimental and simulated curves is overall satisfactory. Notably, the peak position,

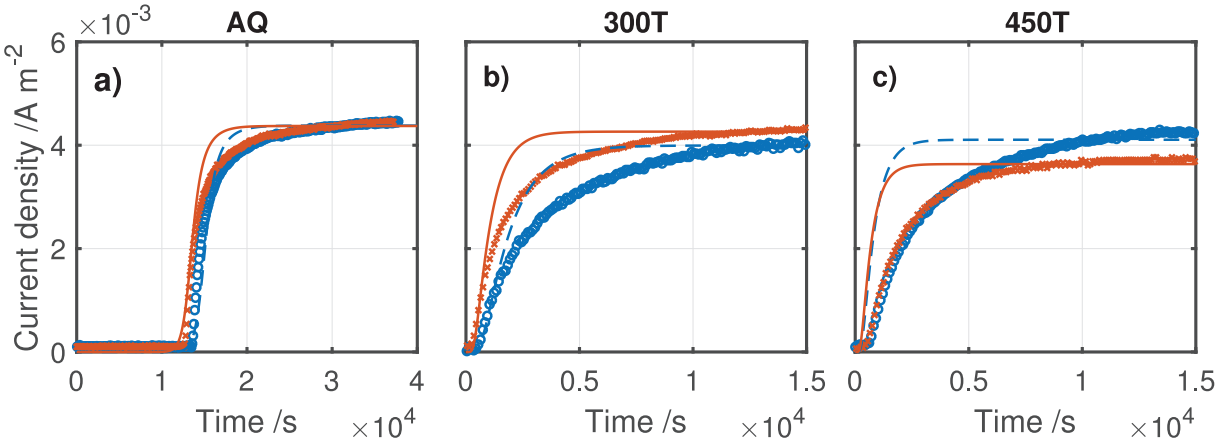

Fig. 7. Experimental and modelled permeation curves using parameters in Table 4. Markers denote experimental data while lines correspond to modelled curves. Thicker samples are marked with open circles and broken lines in blue, while thinner samples are marked with crosses and lines in orange. (For interpretation of the references to colour in this figure legend, the reader is referred to the web version of this article.)

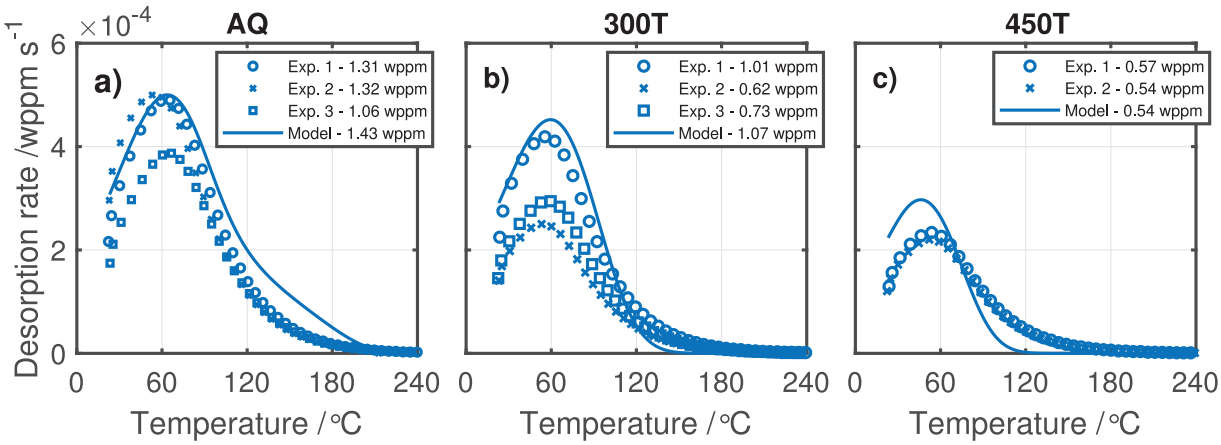

Fig. 8. Experimental and modelled thermal desorption curves using the same trapping parameters as in permeation simulations (see Table 4 – the N_{RA} value was assumed to be 1.7 mol m^{-3}, the same as in the thick AQ permeation sample). Also shown are total measured H concentration values.

which is sensitive to N_t and ΔE_t values and independent of the H lattice concentration, *i.e.* H charging conditions [65], is quite close to experiments. An interesting observation is that the modelled AQ curve, unlike the experimental one, has a shoulder at around 150 °C. This is a reflection of strong traps assumed in the simulations and at odds with experiments. However, based on permeation results we demonstrated that when assuming point trapping and local equilibrium, a strong trapping site is necessary to explain the H permeation behaviour in the AQ condition. A possible explanation for the lack of a high-temperature shoulder in the experimental curves in Fig. 8a could be that the retained austenite starts decomposing and releasing the hydrogen trapped in it. While no measurements of the austenite decomposition kinetics were performed, its effect on H diffusion is an interesting problem that can be modelled. The derivation of the diffusion model extension, along with modelling results using different RA decomposition kinetics, are described in the appendix. Our simulations in Fig. 10 indicate that austenite decomposition at moderate dissolution rates produces small changes in the height of the peak and slightly flattens the shoulder in the curve; it does not however cause a shift in the peak position. A handful of existing studies suggests that decomposition only starts above some 200 °C [66,67], which would require a decomposition a constant smaller than 0.0035 °C^{-1}, although the steels studied were different and the starting temperature may vary significantly with composition. A more likely explanation is that the point trap assumption for RA is not appropriate and the H is contained in the bulk. In this case, barring the presence of a large energy barrier at the austenite-ferrite interface, H would likely start effusing at relatively low temperatures and therefore not generate a high-temperature peak. It is also worth noting that, although austenite decomposition could have changed the TDA behaviour somewhat, our finding of austenite lowering the effective H diffusivity in martensite is based on permeation results. These were conducted at room temperature – therefore the RA fraction was unlikely to change.

Table 5
Dislocation density ρ and grain size d_g in microstructures studied by Mine et al. [18]. HPT stands for high-presssure torsion.

	ρ /m^{-2}	d_g/nm
HPT	2.65×10^{15}	125
HPT + 573K anneal	1.69×10^{14}	167
HPT + 673K anneal	2.89×10^{13}	239
HPT + 773K anneal	1.12×10^{11}	395

3.5. Comparison to the literature

It is also worth drawing a comparison to some previous work on the effect of dislocations and GBs to evaluate the robustness of the trap density scaling laws proposed as well as the choice of ΔE_t for the different traps. While a number of authors investigated the effect of strain on H absorption and the shape of thermal desorption curves [68–73], little information on the microstructure was given in these studies and any changes in H absorption are likely due to a combined effect of vacancies, dislocations and grain refinement. The only thorough study found was by Mine et al. [18,74] who studied ferrite deformed using high-pressure torsion. They characterised both the grain size as well as the dislocation density and studied the H trapping behaviour by gas charging and TDA. The defect densities of the microstructures studied are reported in Table 5.

The samples used by Mine et al. were rectangular, 0.6 mm thick and charged at 358 K in a H atmosphere of 100 MPa, resulting in an equilibrium lattice concentration c_l of 0.55 mol m^{-3} [75]. They were degassed at room temperature for 0.42 h prior to the start of TDA which was conducted under a heating rate of 0.5 K s^{-1}.

We simulated the TDA experiments from [74] with two different sets of parameters – those used for the diffusion simulations in the previous section and those proposed in [74]. Both sets of trap densities together with the corresponding grain size and dislocation density are displayed in Table 6. Note that Mine et al. used binding energy values of 26.0 kJ mol^{-1} and 19.7 kJ mol^{-1} for dislocations and GBs, respectively as well as a somewhat higher value of N_l – 8.64×10^5 mol m^{-3}. The results of both simulations are shown in Fig. 9. Our parameters, despite somewhat overestimating the H concentration, produced a reasonable fit, particularly for their more heavily deformed samples. This is obvious when compared to the H concentrations resulting from the trapping parameters reported by Mine et al. which underestimate the total H concentration by several orders of magnitude. Note that Mine et al. [74] estimated the quality

Table 6
Dislocation density, grain size and the corresponding trap densities in microstructures studied by Mine et al. [18]. HPT stands for high-presssure torsion.

Condition	ρ /m^{-2}	d_g/nm	N_{dis} /mol m^{-3}		N_{GB} /mol m^{-3}	
			Mine et al.	Ours	Mine et al.	Ours
HPT	2.65×10^{15}	125	457	2700	6120	638
HPT + 573K anneal	1.69×10^{14}	167	28.8	170	4780	477
HPT + 673K anneal	2.89×10^{13}	239	4.91	29	3320	334
HPT + 773K anneal	1.12×10^{11}	395	0.02	0.10	1660	202

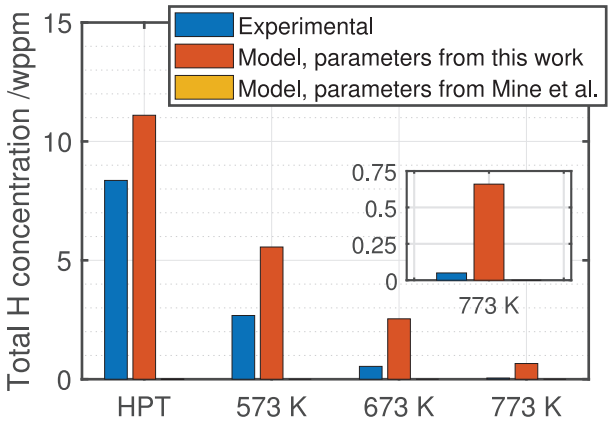

Fig. 9. Comparison of experimental and modelled H concentrations resulting from TDA based on the microstructural data from [18,74]. Note that using the trapping parameters from the latter results in H concentrations too low to be visible in the figure.

of their parameters using the equation for local equilibrium (Eq. (9)) and did not consider the loss of H during the transfer time of 0.42 h which must have been significant given the size of their samples – in our simulations c_l decreased by a factor of 2–10 during this time, depending on the trap density. It is not entirely clear why the discrepancy between the experiments and simulation increases with tempering temperature – the method for estimating dislocation density used in [18] is somewhat simplistic and perhaps underestimates the density at higher tempering temperatures due to dislocation reconfiguration and recovery.

4. Discussion

In this study we integrated microstructural characterisation and H diffusion measurements together with diffusion modelling in a systematic manner in order to identify the variation in H trap density as a function of defect density (GBs and dislocations). One distinct advantage of this approach over the standard single-trap permeation curve analysis using Eqs. (4)–(6), used in numerous studies to date, is that by carefully quantifying the microstructure and varying one parameter (dislocation density) while keeping others (GB area) constant, is that it allows for the identification of scaling laws (trap density as a function of defect density). Moreover, a multi-trap rather than single-trap model is needed to subtract the effect of grain boundaries from other trapping effects. The diffusion parameters identified this way were shown to be valid for martensitic steels and heavily deformed ferrite. Modelling also provides a means of cross-validating experimental data to ensure the inferred trapping parameters are consistent. This way, any phenomena not matching the initial assumptions in the analysis can be identified and studied in more detail. In this paper, that was the effect of RA on H trapping which seems to be inconsistent with the local equilibrium assumption; it was only possible to identify this behaviour by carefully quantifying the trapping contribution of other defects present in martensite.

We should note that the analysis used a number of assumptions, but the validity of each one was carefully assessed. For example, one is the assumption that defects in martensite are point traps. This is justified in Section 2.5 and validated in Section 3.4. Another example is the choice of binding energy of GBs. Since the scatter in reported values in atomistic literature is appreciable, the choice is bound to be somewhat arbitrary. However, 30 kJ mol^{-1} was chosen as it was the average of the reported values analysed. Finally, the choice of boundary condition for the H charging prior to the TDA simulation was chosen to correspond to the total H concentration measured. We initially attempted to calibrate it using information from the literature but the correspondence was poor. Future studies would benefit from a more accurate determination of the above parameters. The average GB binding energy could probably be determined with a combination of DFT and kinetic Monte Carlo methods as previously done for dislocations [52] and more care should be taken to ensure that charging conditions for different experiments (thermal desorption and permeation) are identical. This could be explored in future work.

Having derived a set of scaling laws related to the trapping parameters of GBs and dislocations, we were able to reproduce our experimental results with the H diffusion model, along with additional experimental data from the literature. While there are some discrepancies between the data and the model, the overall trends are reproduced quite well. While some MX carbides were present in the steel studied, they were too sparse to have a notable effect on diffusion. Regardless, adding the effect of carbides is straightforward as the model can accomodate an arbitrary number of distinct traps and we have previously calibrated a trap density correlation for vanadium carbides [8] which could be used for this purpose.

Microstructural characterisation revealed that the dislocation density was nearly identical in the AQ and 300T samples, but was lower by about a factor of 2.5 in the 450T samples. Apart from the limited coarsening of cementite in the two tempered conditions, the only other significant microstructural difference between tempered and AQ samples was the presence of a small amount of RA in the AQ condition. These results imply that the large relative decrease in effective diffusivity in the AQ condition cannot be ascribed to the effect of dislocations. In addition, given the negligible difference in permeation behaviour between the two tempered conditions and an observable, but small difference in H absorption measured by TDA imply that the impact of dislocations on the overall diffusion behaviour is in fact low. This runs somewhat contrary to the received wisdom, but is not surprising given the low binding energy of dislocations recently demonstrated elsewhere [52]. Furthermore, the effect of dislocations was also demonstrated to be low by using the diffusion model to simulate both the experimental permeation curves as well as TDA data. The model was further used to demonstrate that, assuming point traps under local equilibrium, the reduction in diffusivity in the AQ condition could only be ascribed to the presence of a strong and sparse trap. Based on microstructural characterisation, this is most likely RA. The reduction in effective diffusivity in the tempered conditions relative to pure ferrite can be ascribed largely to the presence of GBs. Thermal desorption experiments support these findings – the two tempered conditions were shown to absorb similar H concentrations while the as-quenched microstructure absorbed significantly more.

Microstructural observations and the diffusion behaviour indicate that the RA cannot be approximated as a point trap – to do so results in inconsistencies when attempting to simulate TDA and permeation experiments. This is likely a consequence of bulk trapping in RA – given its volume fraction in the AQ samples and its H solubility ratio with respect to ferrite are such that the resulting trapped hydrogen should be close to the values measured by TDA. The solubility ratio of H between austenite and ferrite is on the order of 10^3 – this is supported by experimental data (see solubility data collected in [76]), and also by recent DFT calculations which show that the energy of H segregation in austenite relative to ferrite is in the range of 10–20 kJ mol^{-1} [48,77]. This means that austenite cannot be anywhere close to saturation given the low H lattice concentration in the ferrite matrix. Using, for example, a value of 19 kJ mol^{-1} in the Arrhenius expression yields a similar solubility ratio as the one used here, ~2000. In our TDA simulations, the H lattice concentration c_l was in the range of 0.08 mol m^{-3}. The corresponding equilibrium H concentration in RA is a product of the solubility ratio, taken as 2×10^3, the volume fraction of austenite, 0.035, and the c_l of ferrite. The resulting value is in the range of 5.6 mol m^{-3} or 0.72 wppm. This is only slightly higher than the measured differences in H concentration between the AQ samples containing RA and the RA-free tempered samples. These considerations demonstrate the need for a 2D

diffusion model, in which bulk trapping in austenite can be accounted for and is presented in part II of this series.

5. Conclusions

- We quantified the hydrogen trap density and H diffusion behaviour in martensite resulting from the presence of dislocations, grain boundaries and retained austenite. Detailed information of the microstructure and its trapping behaviour allowed us to deconvolve for the first time key microstructural features affecting H diffusion in martensite, which contains multiple traps of different densities.
- A set of scaling laws for H trap density based on grain size and dislocation density were proposed and verified by a combination of thermal desorption and permeation experiments coupled with diffusion simulations. The laws are in good agreement with the data presented in the paper as well as data from other sources. The scaling laws are a means towards more accurate modelling of H diffusion and embrittlement susceptibility in steels in the future.
- It was demonstrated that in martensite and heavily deformed ferrite, where the average grain size is small, grain boundaries are more potent trapping sites than dislocations, even at dislocation density values beyond 10^{15} m^{-2}, which is somewhat at odds with previous work.
- Retained austenite has a large impact on H diffusivity and the total absorbed H concentration. Furthermore, the discrepancy between the observed microstructure and the permeation and thermal desorption results shows that retained austenite is unlikely to act as a point trap despite the relative thinness of austenite films. This indicates that a more accurate diffusion model in at least 2D is needed where austenite is treated explicitly and the effect of its morphology on diffusion can be studied in more detail.

Declaration of Competing Interest

None.

Acknowledgements

We gratefully acknowledge the funding received from the HEmS project (grant number EP/L014742/1) and the EPSRC-Rolls Royce strategic partnership (EPSRC grant numbers EPSRCEP/H022309/1 and EP/H500375/1). E. I. Galindo-Nava acknowledges the Royal Academy of Engineering for his research fellowship funding and A. Turk would like to thank Shaumik Lenka, Peng Gong and Tamás Ungár for assistance with experimental work. We thank Diamond Light Source for beamtime (proposal EE17484), and the staff of beamline I11 for assistance with data collection.

Appendix

Model extension to retained austenite decomposition

To account for the thermal decomposition of austenite, the diffusion model used in the study needs to be slightly modified. We shall assume that the loss of trap density corresponding to RA follows an exponential function of the form

$$N_{RA} = N_{RA,0}\exp(-A\Delta T) \tag{13}$$

where $N_{RA,0}$ is the initial RA trap density, A is decomposition a constant and $\Delta T = (T_0 + \phi t) - T_0 = \phi t$. Since trap molar volume V_{RA} is $1/N_{RA}$, this can be rewritten as

$$V_{RA} = V_{RA,0}\exp(A\Delta T) \tag{14}$$

Eqs. (13) and (14) are a simplified form of the JMAK equation using temperature instead of time in the exponential function.

Let us first recall that the total concentration of H in the metal can be split into the lattice H and H trapped at various defects

$$c = c_l + \sum_{k=1}^{m} c_{tk} \tag{15}$$

and that the H in the lattice and in all traps are in local equilibrium

$$c_t = \frac{V_l}{V_t}\frac{c_l}{K_t + c_l V_l(1-K_t)} \tag{16}$$

Using Fick's first law for flux and assuming no diffusion along traps, the mass conservation equation can be written as

$$\frac{\partial}{\partial t}\left(c_l + \sum_{k=1}^{m} c_{tk}\right) = \frac{\partial}{\partial x}\left(D_l\frac{\partial c_l}{\partial x}\right) \tag{17}$$

Previously, c_t was substituted using Eq. (16), accounting for the fact that K_t and c_l were time-dependent. Now, the additional dependency of the inverse trap density, V_t, on time must be considered. c_t is therefore a function of three time-dependent parameters (it is more proper to treat the sum of V_t and V_t as a conserved quantity as in [41], but since $V_t \gg V_l$, this distinction is insignificant)

$$c_t = f\left(K_t\left(T(t)\right), c_l(t), V_t(t)\right) \tag{18}$$

The total derivative of the c_t in time associated to a trap is therefore

$$\frac{dc_t}{dt} = \frac{\partial c_t}{\partial K_t}\frac{\partial K_t}{\partial T}\frac{\partial T}{\partial t} + \frac{\partial c_t}{\partial c_l}\frac{\partial c_l}{\partial t} + \frac{\partial c_t}{\partial V_t}\frac{\partial V_t}{\partial t} \tag{19}$$

where the last term is zero for non-decomposing traps.

Inserting Eqs. (16) and (14) into (19) and the combined expression into (17) the diffusion equation reads

$$\begin{aligned}\frac{\partial c_l}{\partial t} = &\left(1 + \sum_{k=1}^{m}\frac{V_l}{V_{tk}}\frac{K_{tk}}{\left(K_{tk} + V_l c_l(1-K_{tk})\right)^2}\right)^{-1} \\ &\left(\frac{\partial}{\partial x}\left(D_l\frac{\partial c_l}{\partial x}\right) - \sum_{k=1}^{m}\left(\frac{1}{V_{tk}}\frac{c_l^2V_l^2 - c_lV_l}{\left(K_{tk} + V_l c_l(1-K_{tk})\right)^2}\frac{K_{tk}\Delta E_{tk}\phi}{RT^2}\right)\right. \\ &\left. + \frac{V_l}{V_{RA}^2}\frac{c_l}{K_{RA} + V_l c_l(1-K_{RA})}V_{RA,0}A\phi\exp(A\phi t)\right)\end{aligned} \tag{20}$$

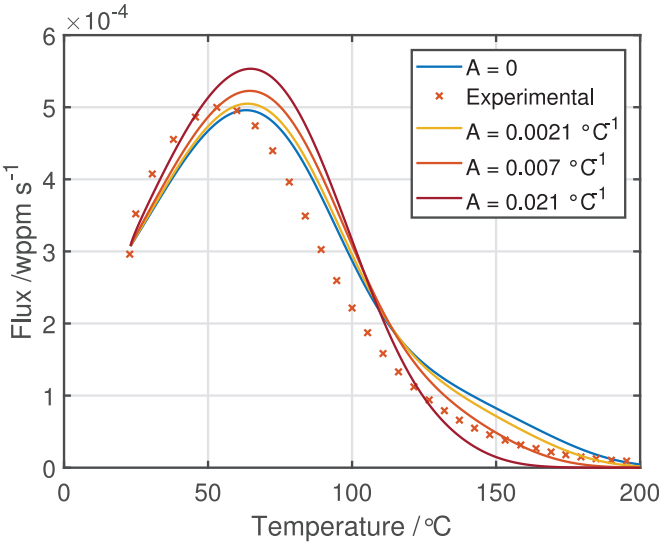

Fig. 10. Effect of RA decomposition on the simulated TDA curves of the AQ condition.

Eq. (20) can now be used to re-examine the TDA curves of the as-quenched (AQ) samples containing RA. Since the exact decomposition kinetics are unknown and no literature was found on steels similar to the one studied here, a brief parametric analysis is shown in Fig. 10, where $A = 0.007\ ^{\circ}C^{-1}$ corresponds to the decomposition of 50% of RA at 100 °C. With increasing A, the decomposition rate increases, reducing the high-temperature tail and increasing the TDA peak, as the overall effusion rate rises, *e.g.* $A = 0.0035\ ^{\circ}C^{-1}$ corresponds to the decomposition of 50% of RA at 200 °C. All the other simulation parameters were the same as in the study.

References

[1] K. Chang, J. Gu, H. Fang, B. Bai, W. Zhang, Z. Yang, D. Liu, C. Zhang, Effect of morphology for novel bainite/martensite dual-phase high strength steel on its hydrogen embrittlement susceptibility, J. Iron. Steel Res. Int. 8 (1) (2001) 37–40.

[2] D. Pérez Escobar, K. Verbeken, L. Duprez, M. Verhaege, Evaluation of hydrogen trapping in high strength steels by thermal desorption spectroscopy, Mater. Sci. Eng. 551 (2012) 50–58, doi: 10.1016/j.msea.2012.04.078.

[3] W. Zhao, T. Zhang, Y. Zhao, J. Sun, Y. Wang, Hydrogen permeation and embrittlement susceptibility of X80 welded joint under high-pressure coal gas environment, Corros. Sci. 111 (2016) 84–97, doi: 10.1016/j.corsci.2016.04.029.

[4] S. Ifergane, E. Sabatani, B. Carmeli, Z. Barkay, V. Ezersky, O. Beeri, N. Eliaz, Hydrogen diffusivity measurement and microstructural characterization of custom 465 stainless steel, Electrochim. Acta 178 (2015) 494–503, doi: 10.1016/j.electacta.2015.08.016.

[5] D.C.S. Garcia, R.N. Carvalho, V.F.C. Lins, D.M. Rezende, D.S. Dos Santos, Influence of microstructure in the hydrogen permeation in martensitic-ferritic stainless steel, Int. J. Hydrogen Energy 40 (47) (2015) 17102–17109, doi: 10.1016/j.ijhydene.2015.06.102.

[6] F.D. Fischer, G. Mori, J. Svoboda, Modelling the influence of trapping on hydrogen permeation in metals, Corros. Sci. 76 (2013) 382–389, doi: 10.1016/j.corsci.2013.07.010.

[7] J. Song, W.A. Curtin, Atomic mechanism and prediction of hydrogen embrittlement in iron, Nat. Mater. 12 (2) (2013) 145–151, doi: 10.1038/nmat3479.

[8] A. Turk, D. San Martín, P.E.J. Rivera-Díaz-del-Castillo, E.I. Galindo-Nava, Correlation between vanadium carbide size and hydrogen trapping in ferritic steel, Scr. Mater. 152 (2018) 112–116, doi: 10.1016/j.scriptamat.2018.04.013.

[9] J.M. Tartaglia, K.A. Lazzari, G.P. Hui, K.L. Hayrynen, A comparison of mechanical properties and hydrogen embrittlement resistance of austempered *vs* quenched and tempered 4340 steel, Metall. Mater. Trans. A 39 (3) (2008) 559–576, doi: 10.1007/s11661-007-9451-8.

[10] N. Eliaz, A. Shachar, B. Tal, D. Eliezer, Characteristics of hydrogen embrittlement, stress corrosion cracking and tempered martensite embrittlement in high-strength steels, Eng. Fail. Anal. 9 (2) (2002) 167–184, doi: 10.1016/S1350-6307(01)00009-7.

[11] X. Li, J. Zhang, J. Chen, S. Shen, G. Yang, T. Wang, X. Song, Effect of aging treatment on hydrogen embrittlement of PH 13-8 Mo martensite stainless steel, Mater. Sci. Eng. 651 (2016) 474–485, doi: 10.1016/j.msea.2015.09.116.

[12] J.L. Gu, K.D. Chang, H.S. Fang, B.Z. Bai, Delayed fracture properties of 1500 MPa bainite/martensite dual-phase high strength steel and its hydrogen traps, ISIJ Int. 42 (12) (2002) 1560–1564, doi: 10.2355/isijinternational.42.1560.

[13] F.-G. Wei, K. Tsuzaki, Response of hydrogen trapping capability to microstructural change in tempered Fe–0.2C martensite, Scr. Mater. 52 (6) (2005) 467–472, doi: 10.1016/j.scriptamat.2004.11.008.

[14] X. Zhu, K. Zhang, W. Li, X. Jin, Effect of retained austenite stability and morphology on the hydrogen embrittlement susceptibility in quenching and partitioning treated steels, Mater. Sci. Eng. 658 (2016) 400–408, doi: 10.1016/j.msea.2016.02.026.

[15] Y. Sakamoto, T. Mantani, Effect of quenching and tempering on diffusion of hydrogen in carbon steel, Trans. Jpn. Inst. Met. 17 (11) (1976) 743–748, doi: 10.2320/matertrans1960.17.743.

[16] S.L.I. Chan, H.L. Lee, J.R. Yang, Effect of retained austenite on the hydrogen content and effective diffusivity of martensitic structure, Metall. Trans. A 22 (11) (1991) 2579–2586, doi: 10.1007/BF02851351.

[17] E.I. Galindo-Nava, P.E.J. Rivera-Díaz-del-Castillo, A model for the microstructure behaviour and strength evolution in lath martensite, Acta Mater. 98 (2015) 81–93, doi: 10.1016/j.actamat.2015.07.018.

[18] Y. Mine, Z. Horita, Y. Murakami, Effect of high-pressure torsion on hydrogen trapping in Fe–0.01 mass% C and type 310S austenitic stainless steel, Acta Mater. 58 (2) (2010) 649–657, doi: 10.1016/j.actamat.2009.09.043.

[19] J. Yang, F. Huang, Z. Guo, Y. Rong, N. Chen, Effect of retained austenite on the hydrogen embrittlement of a medium carbon quenching and partitioning steel with refined microstructure, Mater. Sci. Eng. 665 (2016) 76–85, doi: 10.1016/j.msea.2016.04.025.

[20] S. Takebayashi, T. Kunieda, N. Yoshinaga, K. Ushioda, S. Ogata, Comparison of the dislocation density in martensitic steels evaluated by some x-ray diffraction methods, ISIJ Int. 50 (6) (2010) 875–882, doi: 10.2355/isijinternational.50.875.

[21] T. Ungár, G. Tichy, The effect of dislocation contrast on x-ray line profiles in untextured polycrystals, Phys. Status Solidi (a) 171 (2) (1999) 425–434, doi: 10.1002/(SICI)1521-396X(199902)171:2<425::AID-PSSA425>3.0.CO;2-W.

[22] S.P. Thompson, J.E. Parker, J. Potter, T.P. Hill, A. Birt, T.M. Cobb, F. Yuan, C.C. Tang, Beamline I11 at diamond: a new instrument for high resolution powder diffraction, Rev. Sci. Instrum. 80 (7) (2009) 075107, doi: 10.1063/1.3167217.

[23] T. Ungár, L. Balogh, G. Ribárik, Defect-related physical-profile-based x-ray and neutron line profile analysis, Metall. Mater. Trans. A 41 (5) (2010) 1202–1209, doi: 10.1007/s11661-009-9961-7.

[24] G. Ribárik, B. Jóni, T. Ungár, Global optimum of microstructure parameters in the CMWP line-profile-analysis method by combining Marquardt-Levenberg and Monte-Carlo procedures, J. Mater. Sci. Technol. 35 (7) (2019) 1508–1514, doi: 10.1016/j.jmst.2019.01.014.

[25] B.E. Warren, X-ray studies of deformed metals, Prog. Met. Phys. 8 (1959) 147–202, doi: 10.1016/0502-8205(59)90015-2.

[26] M.A. Krivoglaz, X-Ray and Neutron Diffraction in Nonideal Crystals, Springer Science & Business Media, 2012.

[27] M. Wilkens, Theoretical aspects of kinematical X-ray diffraction profiles from crystals containing dislocation distributions, National Bureau of Standards Fundamental Aspects of Dislocation Theory, Spec. Publ. 317, II, Washington DC, USA, 1970, pp. 1195–1221.

[28] A. Borbély, J. Dragomir-Cernatescu, G. Ribárik, T. Ungár, Computer program ANIZC for the calculation of diffraction contrast factors of dislocations in elastically anisotropic cubic, hexagonal and trigonal crystals, J. Appl. Crystallogr. 36 (1) (2003) 160–162, doi: 10.1107/S0021889802021581.

[29] M.J. Dickson, The significance of texture parameters in phase analysis by X-ray diffraction, J. Appl. Crystallogr. 2 (4) (1969) 176–180, doi: 10.1107/S0021889869006881.

[30] B.D. Cullity, S.R. Stock, Elements of X-Ray Diffraction, Pearson Education, 2014.

[31] HyperSpy: Multi-dimensional data analysis toolbox — HyperSpy, (http://hyperspy.org/).

[32] P.G. Kotula, M.R. Keenan, J.R. Michael, Automated analysis of SEM X-ray spectral images: a powerful new microanalysis tool, Microsc. Microanal. 9 (1) (2003) 1–17, doi: 10.1017/S1431927603030058.

[33] M.A.V. Devanathan, Z. Stachurski, The adsorption and diffusion of electrolytic hydrogen in palladium, Proc. R. Soc. Lond. A 270 (1340) (1962) 90–102, doi: 10.1098/rspa.1962.0205.

[34] A.J. Kumnick, H.H. Johnson, Deep trapping states for hydrogen in deformed iron, Acta Metall. 28 (1) (1980) 33–39, doi: 10.1016/0001-6160(80)90038-3.

[35] M. Nagano, Y. Hayashi, N. Ohtani, M. Isshiki, K. Igaki, Hydrogen diffusivity in high purity alpha iron, Scr. Metall. 16 (8) (1982) 973–976, doi: 10.1016/0036-9748(82)90136-3.

[36] A. McNabb, P. Foster, A new analysis of the diffusion of hydrogen in iron and ferritic steels, Trans. Metall. Soc. AIME 227 (3) (1963) 618–627.

[37] E. Akiyama, S. Li, Electrochemical hydrogen permeation tests under galvanostatic hydrogen charging conditions conventionally used for hydrogen embrittlement study, Corros. Rev. 34 (1–2) (2016) 103–112, doi: 10.1515/corrrev-2015-0049.

[38] S.M. Teus, V.F. Mazanko, J.M. Olive, V.G. Gavriljuk, Grain boundary migration of substitutional and interstitial atoms in α-iron, Acta Mater. 69 (2014) 105–113, doi: 10.1016/j.actamat.2014.01.049.

[39] A. Turk, D. Bombač, J. Jelita Rydel, M. Ziętara, P.E.J. Rivera-Díaz-del-Castillo, E.I. Galindo-Nava, Grain boundary carbides as hydrogen diffusion barrier in a Fe-Ni alloy: a thermal desorption and modelling study, Mater. Des. 160 (2018) 985–998, doi: 10.1016/j.matdes.2018.10.012.

[40] R.A. Oriani, The diffusion and trapping of hydrogen in steel, Acta Metall. 18 (1) (1970) 147–157, doi: 10.1016/0001-6160(70)90078-7.

[41] F.D. Fischer, J. Svoboda, E. Kozeschnik, Interstitial diffusion in systems with multiple sorts of traps, Model. Simul. Mater. Sci. Eng. 21 (2) (2013) 025008, doi: 10.1088/0965-0393/21/2/025008.

[42] H. Kimizuka, S. Ogata, Slow diffusion of hydrogen at a screw dislocation core in α-iron, Phys. Rev. B 84 (2) (2011) 024116, doi: 10.1103/PhysRevB.84.024116.

[43] X. Liu, F. Zhong, J. Zhang, M. Zhang, M. Kang, Z. Guo, Lattice-parameter variation with carbon content of martensite. I. X-ray-diffraction experimental study, Phys. Rev. B 52 (14) (1995) 9970–9978, doi: 10.1103/PhysRevB.52.9970.

[44] Q. Liu, A.D. Atrens, Z. Shi, K. Verbeken, A. Atrens, Determination of the hydrogen fugacity during electrolytic charging of steel, Corros. Sci. 87 (2014) 239–258, doi: 10.1016/j.corsci.2014.06.033.

[45] E. Akiyama, S. Li, Electrochemical hydrogen permeation tests under conventional potentiostatic hydrogen charging conditions conventionally used for hydrogen embrittlement study, ECS Trans. 75 (29) (2017) 23–31, doi: 10.1149/07529.0023ecst.

[46] R.B. Hamzah, M.J. Robinson, Hydrogen absorption resulting from the simulated pitting corrosion of carbon-manganese steels, Corros. Sci. 27 (9) (1987) 971–979, doi: 10.1016/0010-938X(87)90063-1.

[47] L. Vecchi, H. Simillion, R. Montoya, D. Van Laethem, E. Van den Eeckhout, K. Verbeken, H. Terryn, J. Deconinck, Y. Van Ingelgem, Modelling of hydrogen permeation experiments in iron alloys: characterization of the accessible parameters – part II – the exit side, Electrochim. Acta 262 (2018) 153–161, doi: 10.1016/j.electacta.2017.12.173.

[48] Y.A. Du, L. Ismer, J. Rogal, T. Hickel, J. Neugebauer, R. Drautz, First-principles study on the interaction of H interstitials with grain boundaries in α- and γ-Fe, Phys. Rev. B 84 (14) (2011) 144121, doi: 10.1103/PhysRevB.84.144121.

[49] M. Yamaguchi, J. Kameda, K.-I. Ebihara, M. Itakura, H. Kaburaki, Mobile effect of hydrogen on intergranular decohesion of iron: first-principles calculations, Philos. Mag. 92 (11) (2012) 1349–1368, doi: 10.1080/14786435.2011.645077.

[50] D.A. Mirzaev, A.A. Mirzoev, K.Y. Okishev, A.V. Verkhovykh, Ab initio modelling of the interaction of H interstitials with grain boundaries in bcc Fe, Mol. Phys. 114 (0) (2016) 1502–1512, doi: 10.1080/00268976.2015.1136439.

[51] M. Riku, R. Matsumoto, S. Taketomi, N. Miyazaki, Atomistic simulation study of cohesive energy of grain boundaries in alpha iron under gaseous hydrogen environment, J. Soc. Mater. Sci. 59 (8) (2010) 589–595, doi: 10.2472/jsms.59.589.
[52] D. Bombač, I.H. Katzarov, D.L. Pashov, A.T. Paxton, Theoretical evaluation of the role of crystal defects on local equilibrium and effective diffusivity of hydrogen in iron, Mater. Sci. Technol. 33 (13) (2017) 1505–1514, doi: 10.1080/02670836.2017.1310417.
[53] M.J. Peet, T. Hojo, Hydrogen susceptibility of nanostructured bainitic steels, Metall. Mater. Trans. A 47 (2) (2016) 718–725, doi: 10.1007/s11661-015-3221-9.
[54] Y.D. Park, I.S. Maroef, A. Landau, D.L. Olson, Retained austenite as a hydrogen trap in steel welds, Weld. J. 81 (2002) 27S–35S.
[55] A. Turnbull, R.B. Hutchings, Analysis of hydrogen atom transport in a two-phase alloy, Mater. Sci. Eng. 177 (1) (1994) 161–171, doi: 10.1016/0921-5093(94)90488-X.
[56] H. Tsubakino, H. Harada, J. Yin, Thermal release of hydrogen from high strength steel containing retained austenite, ISIJ Int. 39 (3) (1999) 298–300, doi: 10.2355/isijinternational.39.298.
[57] D. Pérez Escobar, T. Depover, L. Duprez, K. Verbeken, M. Verhaege, Combined thermal desorption spectroscopy, differential scanning calorimetry, scanning electron microscopy and x-ray diffraction study of hydrogen trapping in cold deformed TRIP steel, Acta Mater. 60 (6) (2012) 2593–2605, doi: 10.1016/j.actamat.2012.01.026.
[58] R. Nazarov, T. Hickel, J. Neugebauer, First-principles study of the thermodynamics of hydrogen-vacancy interaction in FCC iron, Phys. Rev. B 82 (22) (2010) 224104, doi: 10.1103/PhysRevB.82.224104.
[59] G.-W. Hong, J.-Y. Lee, The interaction of hydrogen and the cementite-ferrite interface in carbon steel, J. Mater. Sci. 18 (1) (1983) 271–277, doi: 10.1007/BF00543835.
[60] W.Y. Choo, J.Y. Lee, Hydrogen trapping phenomena in carbon steel, J. Mater. Sci. 17 (7) (1982) 1930–1938, doi: 10.1007/BF00540409.
[61] D.G. Enos, A.J. Williams, J.R. Scully, Long-term effects of cathodic protection on prestressed concrete structures: hydrogen embrittlement of prestressing steel, Corrosion 53 (11) (1997) 891–908, doi: 10.5006/1.3290274.
[62] D.G. Enos, J.R. Scully, A critical-strain criterion for hydrogen embrittlement of cold-drawn, ultrafine pearlitic steel, Metall. Mater. Trans. A 33 (4) (2002) 1151–1166, doi: 10.1007/s11661-002-0217-z.
[63] D. Di Stefano, M. Mrovec, C. Elsässer, First-principles investigation of hydrogen trapping and diffusion at grain boundaries in nickel, Acta Mater. 98 (2015) 306–312, doi: 10.1016/j.actamat.2015.07.031.
[64] L. Vecchi, H. Simillion, R. Montoya, D. Van Laethem, E. Van den Eeckhout, K. Verbeken, H. Terryn, J. Deconinck, Y. Van Ingelgem, Modelling of hydrogen permeation experiments in iron alloys: characterization of the accessible parameters – part i – the entry side, Electrochim. Acta 262 (2018) 57–65, doi: 10.1016/j.electacta.2017.12.172.
[65] R. Kirchheim, Bulk diffusion-controlled thermal desorption spectroscopy with examples for hydrogen in iron, Metall. Mater. Trans. A 47 (2) (2016) 672–696, doi: 10.1007/s11661-015-3236-2.
[66] T. Waterschoot, K. Verbeken, B.C. De Cooman, Tempering kinetics of the martensitic phase in DP steel, ISIJ Int. 46 (1) (2006) 138–146, doi: 10.2355/isijinternational.46.138.
[67] S. Primig, H. Leitner, Separation of overlapping retained austenite decomposition and cementite precipitation reactions during tempering of martensitic steel by means of thermal analysis, Thermochim. Acta 526 (1) (2011) 111–117, doi: 10.1016/j.tca.2011.09.001.
[68] W.Y. Choo, J.Y. Lee, Thermal analysis of trapped hydrogen in pure iron, Metall. Trans. A 13 (1) (1982) 135–140, doi: 10.1007/BF02642424.
[69] W.Y. Choo, J.Y. Lee, Effect of cold working on the hydrogen trapping phenomena in pure iron, Metall. Trans. A 14 (7) (1983) 1299–1305, doi: 10.1007/BF02664812.
[70] J.-Y. Lee, S.M. Lee, Hydrogen trapping phenomena in metals with B.C.C. and F.C.C. crystals structures by the desorption thermal analysis technique, Surf. Coat. Technol. 28 (3–4) (1986) 301–314, doi: 10.1016/0257-8972(86)90087-3.
[71] H. Hagi, Y. Hayashi, Effect of dislocation trapping on hydrogen and deuterium diffusion in iron, Transactions of the Japan Institute of Metals 28 (5) (1987) 368–374, doi: 10.2320/matertrans1960.28.368.
[72] M. Nagumo, K. Takai, N. Okuda, Nature of hydrogen trapping sites in steels induced by plastic deformation, J. Alloy. Compd. 293 (1999) 310–316, doi: 10.1016/S0925-8388(99)00322-9.
[73] K.-I. Ebihara, T. Suzudo, H. Kaburaki, K. Takai, S. Takebayashi, Modeling of hydrogen thermal desorption profile of pure iron and eutectoid steel, ISIJ Int. 47 (8) (2007) 1131–1140, doi: 10.2355/isijinternational.47.1131.
[74] Y. Mine, T. Tsumagari, Z. Horita, Hydrogen trapping on lattice defects produced by high-pressure torsion in Fe–0.01 mass% C alloy, Scr. Mater. 63 (5) (2010) 552–555, doi: 10.1016/j.scriptamat.2010.05.027.
[75] N.R. Quick, H.H. Johnson, Hydrogen and deuterium in iron, 49–506 C, Acta Metall. 26 (6) (1978) 903–907, doi: 10.1016/0001-6160(78)90041-X.
[76] R. Gangloff, B. Somerday, Gaseous hydrogen embrittlement of materials in energy technologies: the problem, its characterisation and effects on particular alloy classes, number v. 1, Woodhead Publishing Series in Metals and Surface Engineering, Elsevier Science, 2012.
[77] T. Hickel, R. Nazarov, E.J. McEniry, G. Leyson, B. Grabowski, J. Neugebauer, Ab initio based understanding of the segregation and diffusion mechanisms of hydrogen in steels, J. Mater. Sci. 66 (8) (2014) 1399–1405, doi: 10.1007/s11837-014-1055-3.